The Dissertation Committee for Anastassios Andreas Mavrokefalos Certifies that this is the approved version of the following dissertation:

Thermoelectric and Structural Characterization of Individual Nanowires and Patterned Thin Films

Committee:

Li Shi, Supervisor

John R. Howell

Paul S. Ho

Shaochen Chen

Emanuel Tutuc

Thermoelectric and Structural Characterization of Individual Nanowires and Patterned Thin Films

by

Anastassios Andreas Mavrokefalos, B.S.E.; M.S.E.

Dissertation

Presented to the Faculty of the Graduate School of

The University of Texas at Austin

in Partial Fulfillment

of the Requirements

for the Degree of

Doctor of Philosophy

The University of Texas at Austin

December 2008

Dedicated to my family, friends and mentor

Acknowledgements

I am deeply indebted to my advisor, Professor Li Shi, for his constant support. Without his help, this work would never be done. I am thankful to members of my PhD advisory committee who attended my defense: Professor P. S. Ho, Professor J. R. Howell, Professor S. Chen and Professor E. Tutuc. I would like to mention many friends around the campus who have helped me: Dr. Yong Lee, Michael T. Pettes, Arden Moore, Jae Hun Seol, Feng Zhou and others.

Thermoelectric and Structural Characterization of Individual

Nanowires and Patterned Thin Films

Publication No._____

Anastassios Andreas Mavrokefalos, Ph.D.

The University of Texas at Austin, 2008

Supervisor: Li Shi

This dissertation presents the development of methods based on microfabricated devices for combined structure and thermoelectric characterizations of individual nanowire and thin film materials. These nanostructured materials are being investigated for improving the thermoelectric figure of merit defined as $ZT=S^2\sigma T/\kappa$, where S is the Seebeck coefficient, σ is the electrical conductivity, κ is the thermal conductivity, and T is the absolute temperature. The objective of the work presented in this dissertation is to address the challenges in the measurements of all the three intrinsic thermoelectric properties on the same individual nanowire sample or along the in plane direction of a thin film, and in correlating the measured properties with the crystal structure of the same nanowire or thin film sample. This objective is accomplished by the development of a four-probe thermoelectric measurement procedure based on a micro-device to measure the intrinsic κ, σ, and S of the same nanowire or thin film and eliminate the contact thermal and electrical resistances from the measured properties. Additionally the device

has an etched through hole that facilitates the structural characterization of the sample using transmission electron microscopy (TEM) and energy dispersive X-ray spectroscopy (EDS).

This measurement method is employed to characterize individual electrodeposited $Bi_{1-x}Te_x$ nanowires. A method based on annealing the nanowire sample in a forming gas is demonstrated for making electrical contact between the nanowire and the underlying electrodes. The measurement results show that the thermoelectric propertied of the nanowires are sensitive to the crystal quality and impurity doping concentration. The highest ZT found in three nanowires is about 0.3, which is still lower than that of bulk single crystals at the optimum carrier concentration. The lower *ZT* found in the nanowires is attributed to the high impurity or carrier concentration and defects in the nanowires.

The micro-device is further modified to extend its use to characterization of the in-plane thermoelectric properties of thin films. Existing practice for thermoelectric characterization of thin films is obtaining κ in the cross plane direction using techniques such as the 3ω method or time domain laser thermal reflectance technique whereas the σ and *S* are usually obtained in the in-plane direction. However, transport properties of nanostructured thin films can be highly anisotropic, making this combination of measurements along different directions unsuitable for obtaining the actual *ZT* value. Here, the micro-device is used to measure all three thermoelectric properties in the in-plane direction, thus obtaining the in-plane *ZT*. A procedure based on a nano-manipulator is developed to assemble etched thin film segments on the micro-device. Measurement results of two different types of thin films are presented in this dissertation.

The first type is mis-oriented, layered thin films grown by the Modulated Elemental Reactant Technique (MERT). Three different structures of such thin films are characterized, namely WSe_2, $W_x(WSe_2)_y$ and $(PbSe_{0.99})_x(WSe_2)_x$ superlattice films. All three structures exhibit in-plane κ values much higher than their cross-plane κ values, with an increased anisotropy compared to bulk single crystals for the case of the WSe_2 film. The increased anisotropy is attributed to the in-plane ordered, cross-plane disordered nature of the mis-oriented, layered structure. While the WSe_2 film is semi-insulating and the $W_x(WSe_2)_y$ films are metallic, the $(PbSe_{0.99})_x(WSe_2)_x$ films are semiconducting with its power factor ($S^2\sigma$) greatly improved upon annealing in a Se vapor environment.

The second type of thin films is semiconducting InGaAlAs films with and without embedded metallic ErAs nanoparticles. These nanoparticles are used to filter out low energy electrons with the introduction of Schottky barriers so as to increase the power factor and scatter long to mid range phonons and thus suppress κ. The in-plane measurements show that both the S and σ increase with increasing temperature because of the electron filtering effect. The films with the nanoparticles exhibited an increase in σ by three orders of magnitude and a decrease in S by only fifty percent compared to the films without, suggesting that the nanoparticles act as dopants within the film. On the other hand, the measured in-plane κ shows little difference between the films with and without nanoparticles. This finding is different from those based on published cross-plane thermal conductivity results.

Table of Contents

List of Tables

List of Figures

Chapter 1: Introduction

1.1 Thermoelectric transport in nanostructured materials

Solid state refrigeration can be achieved using the Peltier effect, where a current flow across a thermocouple junction can transfer heat. Conversely, a temperature difference across a thermoelectric (TE) material can generate an electric current. The efficiency of a TE device depends on the dimensionless TE figure of merit of the materials defined as $ZT=\sigma S^2 T/\kappa$, where σ is the electrical conductivity, S is the Seebeck coefficient, T is the temperature, and κ the thermal conductivity consisting of a lattice contribution (κ_l) and an electronic contribution (κ_e), i.e. $\kappa=\kappa_l+\kappa_e$. A ZT larger than 3 is needed for TE coolers to be able to compete with vapor compression units. For the past 50 years the best bulk material for TE refrigeration is a bismuth telluride alloy with a ZT close to unity at room temperature. The reason why it has been difficult to increase the value of ZT is because σ, S and κ are interdependent. There is a trade off between σ and S as the dopant concentration is varied and κ_e is proportional to σ according to the Wiedemann-Franz law. It was proposed a decade ago (Hicks et al. 1993, Hicks et al. 1993) that TE power factor ($P=S^2\sigma$) could be increased in low dimensional structures such as quantum wells and wires, by taking advantage of the asymmetric density of states (DOS) near the Fermi level of these structures. Additionally, κ is also reduced in nanostructures due to the increased phonon-boundary scattering rate as well as other possible confinement effects (Chen et al. 2002). The combination of these effects could potentially increase ZT to a value greater than unity. It wasn't until half a decade ago that

ZT enhancement up to the range from 1.5 to 2.5 was reported in thin film superlattices (Harman et al. 2002, Venkatasubramanian et al. 2001). Recently there has also been a breakthrough in the bulk TE materials development (Hsu et al. 2004) where a *ZT* about 2 was reported. Even though it is a bulk material, the increase in the TE figure of merit is attributed to to embedded nanoparticles. Another recent report (Heremans et al. 2008) has also shown that an asymmetric DOS can be realized in bulk materials as well. Through the doping of PbTe system with Thallium, the 3D DOS near the Fermi level was distorted, so that *P* alone was increased without affecting κ. A *ZT* value of 1.5 was reported. It has been speculated that much greater *ZT* enhancement could be achieved by employing phonon scattering mechanisms via nanostructuring.

A lot still needs to be done to understand thermoelectric transport in nanomaterials. Theoretical studies (Broido et al. 1995, Broido et al. 1997, Lin-Chung et al. 1995) have shown that in realistic superlattice systems *ZT* enhancement along the in-plane direction is limited by the following factors: (i) electron tunneling through the barrier layers alters the DOS and limits *P*, (ii) carrier-phonon scattering increases, limiting thus mobility and σ, and (iii) parasitic thermal conduction through the barrier layers further reduces *ZT*. It is suggested that freestanding structures such as nanowires made out of III-V material such as Bi and InSb can be used to obtain high *ZT* (Broido et al. 2001, Lin et al. 2000, Mingo 2004). It was recently reported that Si nanowires (Boukai et al. 2008, Hochbaum et al. 2008) have a *ZT* approaching unity at room temperature. The enhancements were attributed mainly to the phonon suppression due to the size

confinement and diffuse scattering or backscattering of phonons (Moore et al. 2008) due to the surface roughness of the nanowires.

Another approach to enhancing *ZT* is based on solid state thermionic emission. This approach takes advantage of energy barriers provided by heterostructures inside a solid. These energy barriers block low-energy carriers and only allow carriers with enough energy to overcome the barrier height. Moreover, these hetero-structures can also scatter phonons and suppress the thermal conductivity. Zeng et al. (Zeng et al. 2007) has already reported peak ZT values of ~1 at 600K for an III-V hetero-structure. This material is a semiconducting InGaAlAs film grown by Molecular Beam Epitaxy (MBE) with embedded metallic ErAs nanoparticles in the matrix. The metal-semiconductor interfaces gives rise embedded Schottky barriers that block low-energy electrons. Additionally these embedded nanoparticles can scatter the mid-long wavelength phonons without affecting the electrical properties of the film (Kim et al. 2006). The electrical conductivity is also improved by the embedded particles that increase the electron concentration. Although the viability of this approach has been demonstrated, the reported peak ZT~1 was calculated by combining the results of the in-plane σ, S and cross-plane κ. It remains to be verified whether the thermoelectric properties of these materials are isotropic.

1.2 Existing thermoelectric characterization methods

There have been extensive efforts to experimentally verify the predicted *ZT* enhancement in low dimensional systems. Measurement results of *S* and the electrical

resistance (R) of bismuth and bismuth antimony nanowire arrays grown in anodized alumina templates (AAMs) have been reported (Heremans et al. 1999, Lin et al. 2002). Because the sizes and the number of nanowires that contacted the electrodes were unknown, the electrical conductivity σ was not obtained in these measurements. Moreover, the thermal conductivity of the nanowires was not obtained because of thermal leakage through the AAM template. Indeed, it is not a trivial task to measure the intrinsic thermoelectric properties of individual nanowires due to the difficulty in the manipulation of the nanowire samples with the small dimension. While the σ of an individual nanowire can be readily measured, the measurements of S and κ of individual nanowires are very challenging.

Cronin et al. (Cronin et al. 2002) proposed a differential method to measure the S and σ of a single bismuth nanowire. In this method, four electrical contacts were made on top of the nanowire using electron beam lithography (EBL). The σ of the nanowire may be calculated from the measured four probe resistance. An electrical heater was patterned perpendicular and close to one end of the nanowire. In addition, a bismuth film with a thickness comparable to the nanowire diameter was evaporated and patterned into a nanoscale line parallel and close to the nanowire. During the experiment, the electrical heater was used to create a temperature difference (ΔT) across the nanowire as well as the bismuth film. By measuring the thermoelectric voltage (ΔV) across the film and assuming the S of the film to be that of the bulk bismuth, one could calculate the ΔT, which was assumed to be the same for the nanowire and the film. The S of the nanowire could then be obtained by measuring the thermoelectric voltage across the nanowire. In their work,

however, the S and σ of the bismuth nanowire were not obtained due to poor electrical contacts on the nanowire. With the use of a different approach of fabricating a resistance thermometer line to measure the temperature difference across the sample, Small et al. (Small et al. 2003) successfully measured the S of a SWCNT. In principle, this method can be used to measure the S and σ of an individual thermoelectric nanowire.

In addition, a so-called 3ω method has been employed to measure the thermal conductivity of a platinum wire (Lu et al. 2001), a large MWCNT bundle (Yi et al. 1999), and recently an individual MWCNT (Choi et al. 2005). This method relies on the self heating of a suspended wire under a sinusoidal current ($i_0\sin\omega t$) at frequency ω. The sinusoidal current leads to a temperature rise modulated at the second harmonic frequency (2ω). Due to the temperature-dependence of the electrical resistance (R) of the wire, R is also modulated at the 2ω frequency. The voltage drop along the wire is $v = (i_0\sin\omega t)R$ and contains a modulated component ($v3\omega$) at the 3ω frequency. The thermal conductivity κ of the wire is obtained with the use of a well-defined correlation between $v_{3\omega}$ and the thermal conductivity in the low frequency regime. For using this method to measure a nanowire, however, it is important that the nanowire has a good σ and a large temperature coefficient of resistance (TCR). Additionally, the contact electrical resistance needs to be eliminated so that the electrical resistance of the nanowire can be obtained. In four-probe measurement of the electrical resistance of the finest nanowire or nanotube with a diameter on the order of 1 nm, however, the mesoscopic voltage probes are often invasive and can very well be the dominant source of scattering and hence resistance (Datta et al. 1995). Unless very weakly coupling or non-invasive voltage

probes are used in the four probe measurement, the obtained four-probe resistance is not purely the intrinsic resistance of the fine nanostructure and cannot be used to obtain the correct temperature rise in the nanostructure (Datta et al. 1995). Moreover, electrons and phonons need to be at equilibrium during self heating so that resistance thermometry can be employed. In SWCNTs and other nanowires under self heating in a high electric field, electrons and phonons are often not at equilibrium because the length of the nanostructure can become comparable to the mean free paths for scattering between these carriers. This issue is especially the case at low temperatures. Consequently, the 3ω self-heating method cannot be applied to obtain the temperature-dependent thermal properties of these nanostructures.

Recently, a microfabricated device was developed to successfully measure the κ of individual carbon nanotubes (Kim et al. 2001, Yu et al. 2005), Si nanowires (Li et al. 2003), Si/SiGe superlattice nanowires (Li et al. 2003), rough Si nanowires (Chen et al. 2008). In addition, the κ, S, and σ of individual $Bi_{1-x}Te_x$ nanowires have also bee measured using the micro-device (Zhou et al. 2005). The micro-device consisted of two symmetric and adjacent SiN_x membranes that are suspended by five long SiN_x beams. Platinum resistance thermometers (PRT) on each membrane can be used to create and measure the temperature difference across the sample that is electrically contacted with additional Pt electrodes. A modified version of this approach has been utilized to measure the TE properties of Si nanowires (Boukai et al. 2008). In that work, Si nanowires down to 10 nm width and on top of a thin SiO_2 island were patterned from a Silicon on Insulator (SOI) wafer. This island also contains 2 RTs on either side of the nanowire

array to act as heating sources and 2 RTs in contact with the nanowires on either side to measure the temperature drop across the nanowire and perform the electrical measurements. The thermal measurement is based on a differential measurement. The thermal conductance of the nanowires and the SiO_2 island are first measured together. Subsequently, the Si nanowires were etched away and the thermal conductance of the remaining SiO_2 was measured again. The difference of the two measured thermal conductance is taken as the thermal conductance of the Si nanowires. However, the difference between these two values is about 100 times smaller than the two values, and comparable to the measurement uncertainty of the two values.

On the other hand, one of the major challenges in the research of thin film thermoelectric materials is to characterize all the thermoelectric properties of thin films along the same crystal directions and relate them to their crystal structures. These thin films are often highly anisotropic with very different properties along the cross-plane and in-plane directions. While the 3ω method (Cahill 1990) and the time-domain laser reflectance technique (TDLR) (Cahill 2004) have been employed with success to measure the cross-plane thermal conductivity of thin films, measuring the in-plane thermal conductivity of thin films has been difficult because of parasitic heat conduction in the substrate. In the 3ω method for cross-plane thermal conductivity measurement, a metal line is patterned on top of the sample film. The metal line acts as a heater and a thermometer. A sinusoidal current at frequency 1ω is passed through the metal line. The resulting Joule heating is at the 2ω frequency and leads to a temperature fluctuation at the 2ω frequency. This temperature fluctuation causes the metal electrical resistance to

fluctuate at the 2ω frequency as well. Because the voltage drop along the metal line is the product of the current at 1ω frequency and the resistance with a 2ω frequency component, the measured voltage contains a 3ω component. This 3ω component is used to extract the thermal conductivity of the sample at low frequencies. The TDLR technique is based on a laser pump/probe technique. A thin metal film is deposited on top of the film sample. Short laser pulses with a pulse width <1ps for both the pump and the probe beams are delivered to the sample. A photo detector is used to measure the reflected probe beam from the sample. The in phase and out of phase signals are measured by the lock-in and are used to obtain the thermal conductivity information. These data are fitted then to a thermal model where the thermal conductivity is extracted.

To measure the in-plane thermal conductivity, Ju et al. (Ju et al. 1999, Ju et al. 1999) extended the 3ω method to obtain the in-plane thermal conductivity of a thin film by using microfabricated heater bridges of varying widths . The thermal conductivity of the film was extracted by fitting a two-dimensional heat conduction model to the measurement results. To directly measure the in-plane thermal conductivity of silicon thin films, Liu et al. (Liu et al. 2006) patterned the film into a suspended beam and employing a metal layer on top of the patterned film as a heater and resistance thermometer. The uncertainty of the metal layer thickness and thermal conductivity introduces uncertainties to the measured thermal conductivity of the silicon film. Zink et al. (Zink et al. 2005) used a modified microcalorimeter method to obtain the in-plane thermal conductivity of Pb and Au thin films. They evaporated the thin film on the

backside of a SiN$_x$ device and then obtained the thermal conductivity by comparing the thermal conductance before and after the evaporation.

Moreover, it is difficult to accurately measure the cross-plane electrical conductivity and Seebeck coefficient of thin films because of the influence of contact resistance and substrate resistance. Hence, most of the S and σ measurements are in the in-plane direction. For this reason, the ZT values reported by Zeng et al. (Zeng et al. 2007) on thin films with embedded nanoparticles are based on the in-plane P and cross-plane κ. This can create errors when the thin film is anisotropic. Technical issues also exist in measuring the in-plane electrical conductivity and Seebeck coefficient of thin films at high temperature, where the contribution from thermally generated carriers in a semi-insulating substrate cannot be ignored.

1.3   Motivation and Scope of this work

The aim of this work is to address several aforementioned limitations in measuring the TE properties of individual nanowires and thin films. The first issue addressed by this dissertation is measurement of all the three TE properties on the same nanowire or thin film sample. Many reported ZT of nanostructured material to this date are calculated by obtaining S, σ and κ from different samples respectively (Hochbaum et al. 2008). This can lead to errors because of non-uniformity in the samples of the measurements. This problem is overcome by adding two more electrodes to the previous design of the micro-device (Shi et al. 2003), so that the intrinsic S, σ and κ of the same sample can be measured using a four-probe TE measurement procedure developed in this

work. This four-probe method is employed to characterize the TE properties of individual electrodeposited bismuth telluride nanowires.

The second issue addressed by this dissertation is correlating the structural characteristics of the samples to their TE properties. TE properties are very sensitive to crystal quality, stoichiometry, and crystal growth direction. Structural characterization of nanostructures is usually done on different samples from those where the TE properties are obtained, because the TE measurement devices do not allow for such characterization by transmission electron microscopy (TEM). This issue is addressed by creating an etched through hole in the micro-device so that the crystal structure of the sample can be characterized using TEM.

The third issue addressed by this dissertation is measuring all the three in-plane TE properties on the same thin film sample. This is accomplished by extending the micro-device initially developed for nanowires for in-plane measurement of a free-standing thin film assembled on the measurement device. Because the thin film sample was suspended, any substrate contribution was eliminated. This allows for measuring the intrinsic in-plane TE properties of the thin film. The in-plane thin film measurement method is demonstrated using disordered, layered films (Mavrokefalos et al. 2007) and InAlGaAs films with and without embedded ErAs nanoparticles.

Chapter 2: Development of Methods for Combined Structure and Thermoelectric Characterization of Nanowires and Thin Films

This chapter presents the development of a batch fabricated micro-device for combined structure and thermoelectric characterization of individual nanowires and patterned thin films.

2.1   Design and Fabrication of the Measurement Device

A shown in Fig. 1, the device consists of two adjacent 20 μm x 20 μm low-stress silicon nitride (SiN_x) membranes each suspended with six 420-μm-long and 2-μm-wide SiN_x beams. One platinum serpentine resistance thermometer (PRT) and two Pt electrodes were patterned on each membrane. The fabrication method was modified from that for the previous design (Shi et al. 2003). Firstly, the new design of the device contains four Pt electrodes instead of only two Pt electrodes in the previous design, so that all the three TE properties can be measured with a four probe method that eliminates both the contact thermal and electrical resistances. Secondly, wafer-scale electron beam lithography (EBL) and sputter etching were used to pattern the two PRTs and the four Pt electrodes on each device from a Pt thin film deposited on the SiN_x film, followed by a photolithography and sputter etching step to pattern the twelve long Pt leads and contact pads. The use of EBL allowed us to reduce the linewidth of the PRT to about 100-200 nm so that the electrical resistance of the PRT is about four times higher than that of the two long Pt leads connected to the PRT. Lastly, for the current design, an additional back-side patterning step was used to open etching windows in the back-side SiN_x, so that the Si substrate under the suspended device can be etched through in a tetramethylammonium

11

hydroxide (TMAH). With the added etch-through hole, the crystal structure and chemical composition of the nanowire or thin film sample assembled on the suspended device can be measured using TEM and the energy dispersive X-ray spectroscopy (EDS) capability of the TEM, respectively.
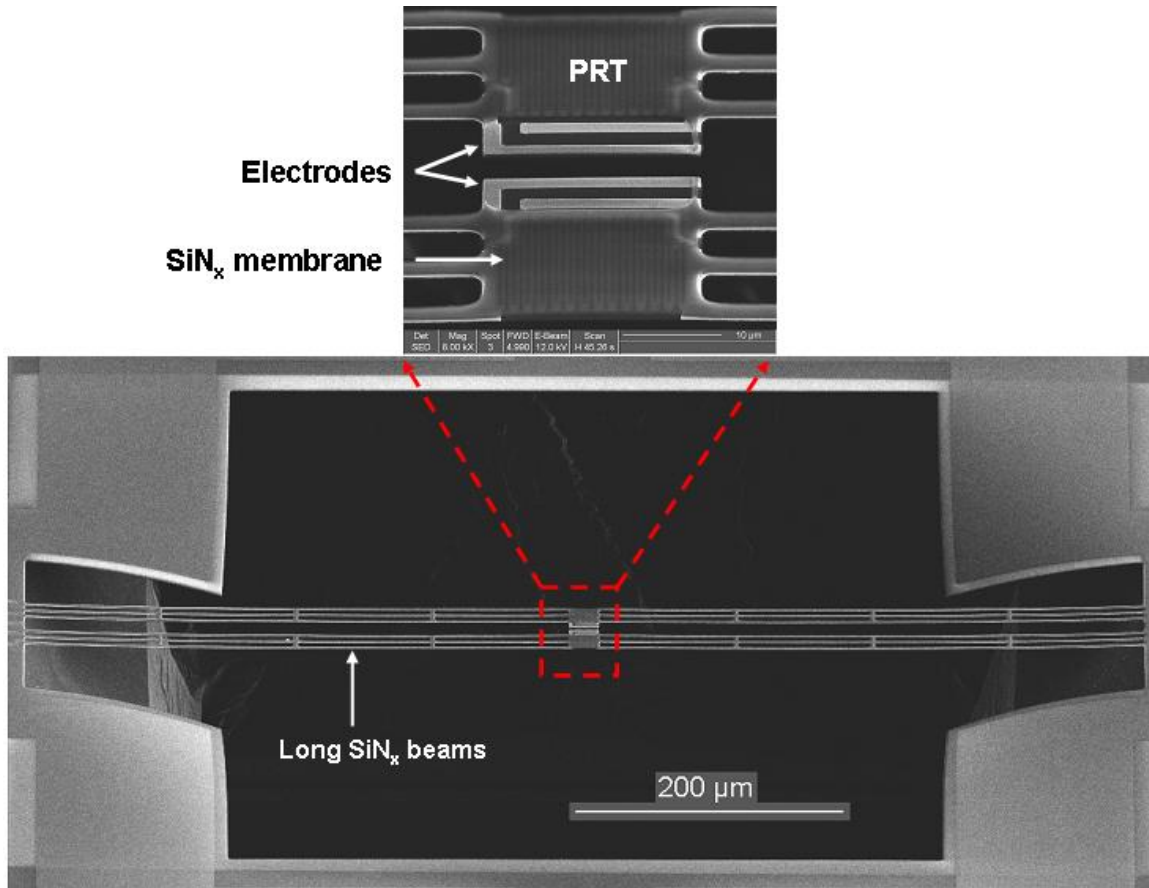
Fig. 1: SEM image of the microdevice for measuring thermal properties of nanostructures

2.2   Four-probe Thermoelectric Measurement Method

The thermoelectric measurements were conducted in a Janis ST-100 continuous flow liquid Helium cryostat where the sample space is in high vacuum and the temperature range is 4 to 800 K. The thermal resistance of the nanofilm sample was

obtained based partly on the procedure developed previously for nanowire samples (Shi et al. 2003, Shi et al. 2005, Zhou et al. 2005). When a direct current (I) was supplied to one PRT to raise the temperature of one membrane, part of the Joule heat generated in the heating membrane, Q, was conducted through the sample to the other (sensing) membrane, as shown in Fig. 2. Because the internal thermal resistance of each membrane is on the order of 10^5 K/W and is two orders of magnitude smaller than the thermal resistance of the six beams supporting each membrane, the temperature distribution on each membrane is uniform during the heating process. The temperature uniformity has been verified in a finite element calculation (Yu et al. 2006).
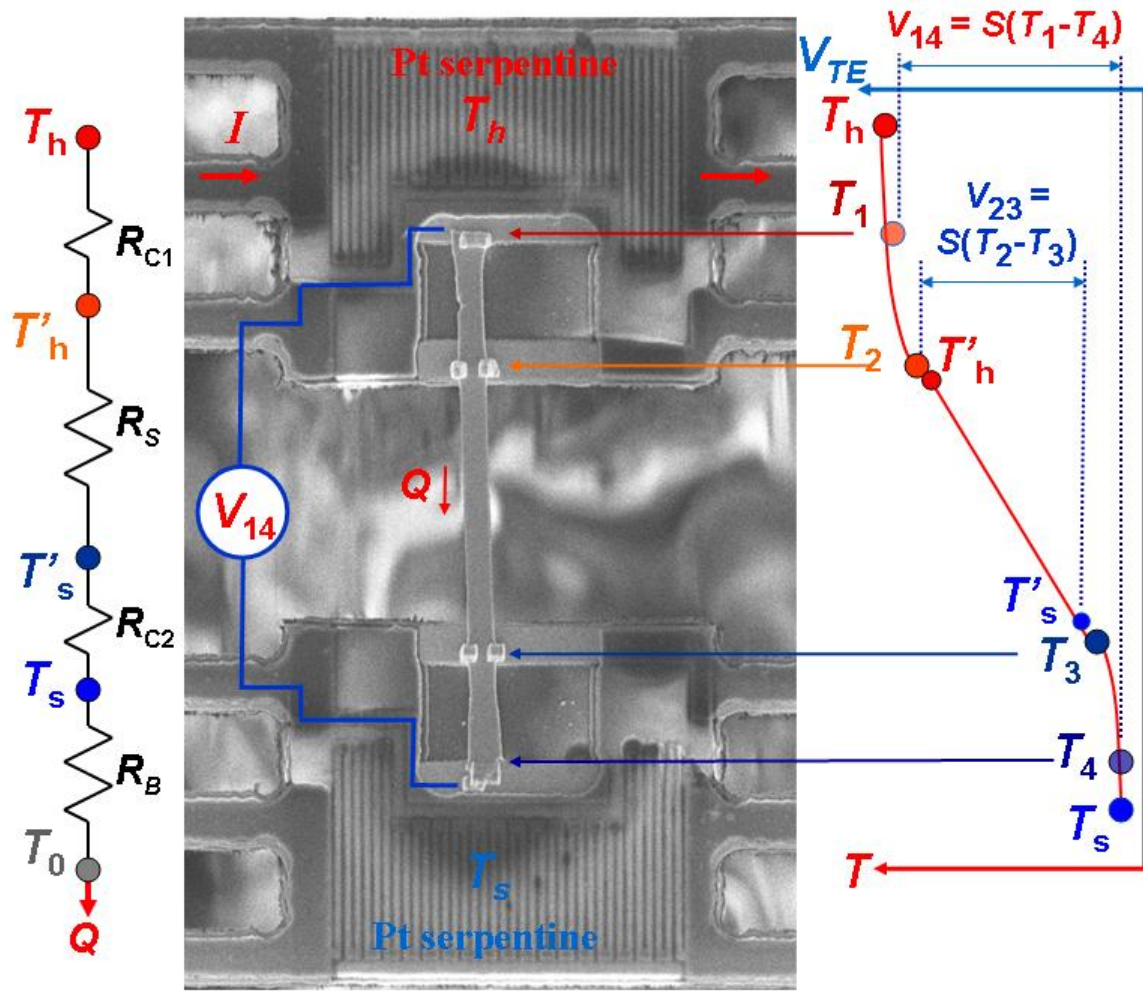
Fig. 2: A schematic diagram of the thermal measurement methods. T_h and T_s are the temperatures of the heating (upper) and sensing (lower) membranes, respectively. T_1, T_2, T_3, and T_4 are the temperatures at the four contacts between the sample and the narrow Pt patterns deposited on the sample. T_0 is the temperature of the substrate. R_s and R_B are the thermal resistances of the sample and the six beams supporting one membrane, respectively. R_{C1} and R_{C2} are the contact thermal resistances between the sample and the heating and sensing membranes, respectively. V_{14} and V_{23} are the thermoelectric voltages (V_{TE}) measured between the two outer and between the two inner electrodes, respectively

The two PRTs were used to measure the temperature rises on the heating and sensing membranes at different I values, $\Delta T_h(I) \equiv T_h(I) - T_0$ and $\Delta T_s(I) \equiv T_s(I) - T_0$, respectively, where T_0 is the substrate temperature. The thermal resistance (R_B) and thermal conductance (G_B) of the six beams supporting each membrane was obtained as

$$R_B = G_B^{-1} = \frac{\Delta T_h + \Delta T_s}{Q_h + Q_l} \qquad (2.1)$$

where Q_h is the Joule heat dissipation in the PRT on the heating membrane, and Q_l is the Joule heat dissipation in one of the two identical Pt leads supplying the current to the heating PRT. The R_B is obtained from the slope of the $\Delta T_h + \Delta T_s$ versus $Q_h + Q_l$ curve, as shown in Fig. 3 for $T_0 = 400K$.
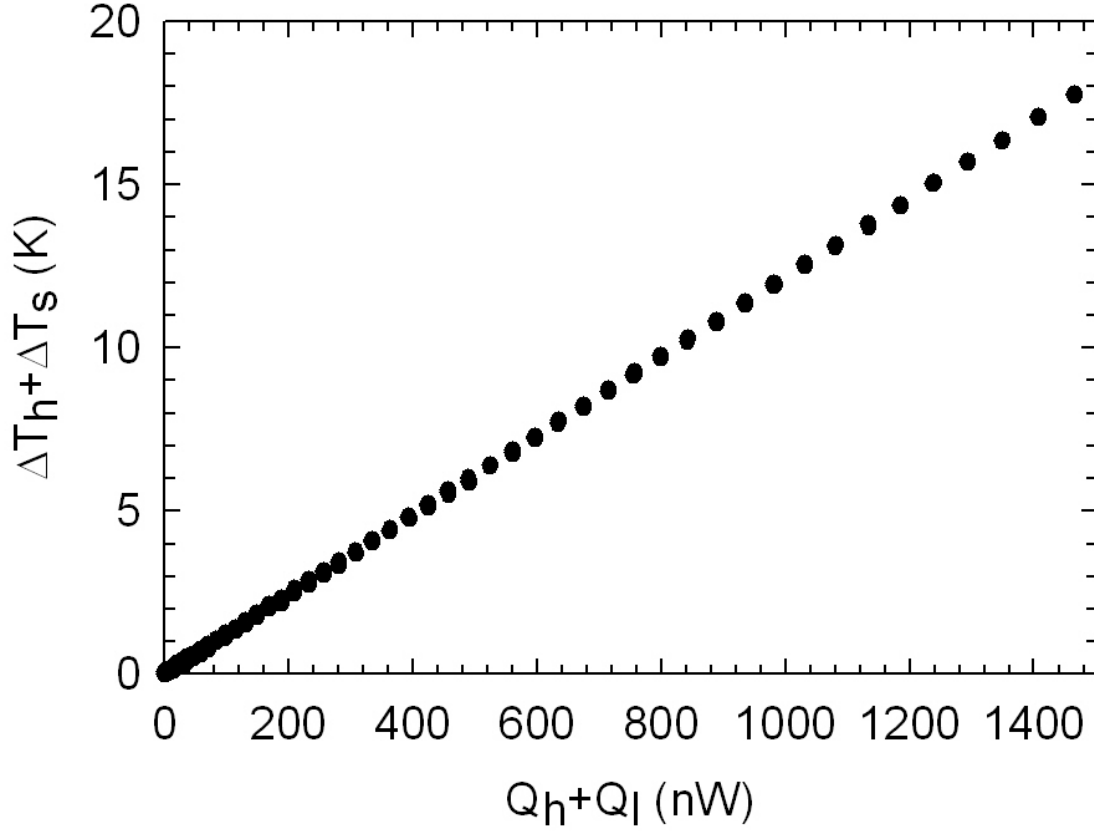
Fig. 3: Measured $\Delta T_h + \Delta T_s$ as a function of $Q_h + Q_l$. The slope yields R_B of the five beams supporting one membrane on the microdevice at $T_0 = 400K$

According to the thermal circuit in Fig. 2, the total thermal resistance (R_{total}) and thermal conductance (G_{total}) were obtained as

$$R_{total} = G_{total}^{-1} = R_{C1} + R_S + R_{C2} = \frac{\Delta T_h - \Delta T_s}{Q} \tag{2.2}$$

where R_S is thermal resistance of the suspended nanofilm or nanowire sample, R_{C1} and R_{C2} are the two contact thermal resistances. Because the heat loss from the sample by radiation was several orders of magnitude smaller than heat conduction through the

sample, Q equals the heat conducted through the six beams of the sensing membrane to the substrate, which was obtained as

$$Q = R_B \Delta T_s \qquad (2.3)$$

Hence,

$$R_{total} = G_{total}^{-1} = \frac{\Delta T_h - \Delta T_s}{\Delta T_s} R_b \qquad (2.4)$$

The obtained ΔT_h-ΔT_s vs ΔT_s for T_o=400K is shown in Fig. 4.
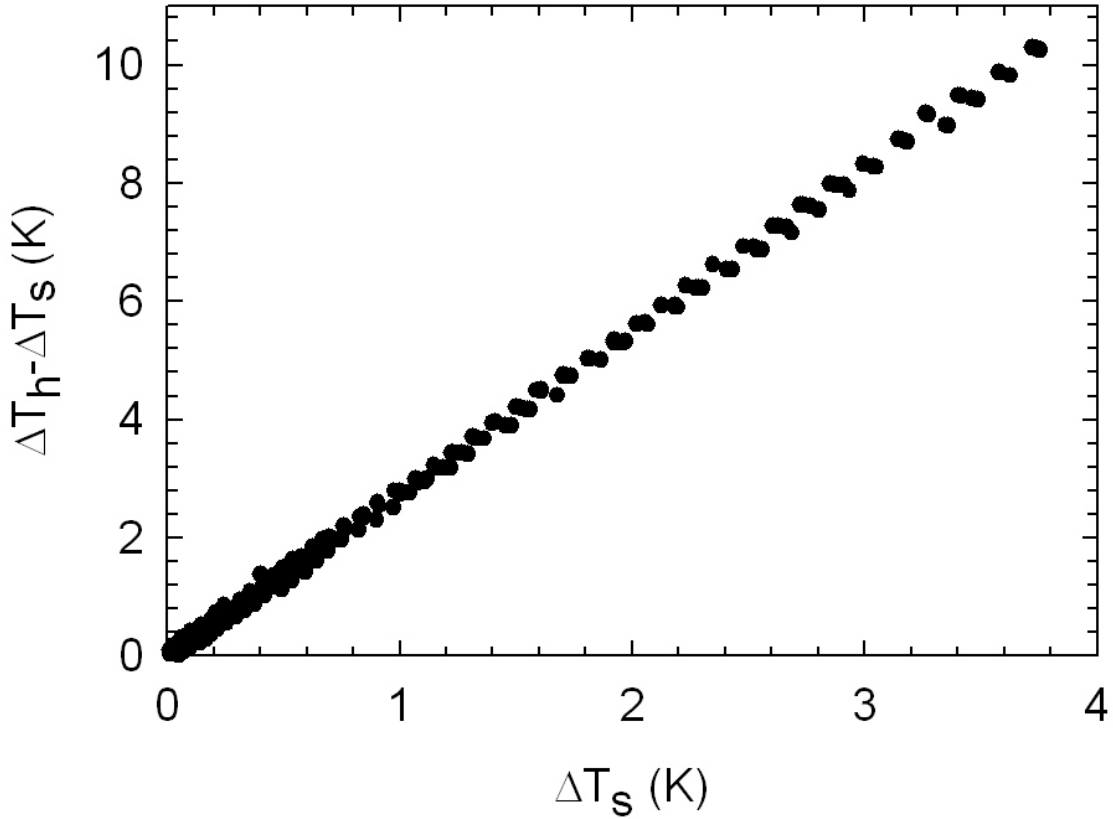
Fig. 4: The obtained ΔT_h-ΔT_s vs ΔT_s at T_o=400K.

The new design of the microdevice allowed us to obtain the total contact thermal resistance ($R_{C1} + R_{C2}$) between the suspended sample and the two PRT membranes. According to the temperature profile schematic shown in Fig. 2, the contact thermal resistances could cause temperature drops, i.e. ($T_h - T_h'$) and ($T_s' - T_s$), where T_h' and T_s' were the temperatures at the two ends of the suspended segment of the nanofilm. While the temperature profile was linear between T_h' and T_s' along the suspended segment, the temperature decayed approximately exponentially between T_h' and T_1 and between T_s' and T_4 because of heat transfer between the nanofilm and the membrane in contact, where T_1 and T_4 were the temperatures of the sample at the two outer electrodes shown in Fig. 2. The temperature differences ($T_1 - T_4$) and ($T_2 - T_3$) resulted in two thermoelectric voltages that could be measured between the two outer electrodes and between the two inner electrodes,

$$V_{14} = S(T_1 - T_4) \tag{2.4a}$$

and

$$V_{23} = S(T_2 - T_3) \tag{2.4b}$$

where S is the Seebeck coefficient of the nanofilm or nanowire sample and is assumed to be uniform along the sample. We define

$$S_{14} \equiv V_{14} / (T_h - T_s) \tag{2.5a}$$

and

$$S_{23} \equiv V_{23} / (T_h - T_s) \tag{2.5b}$$

so that

$$\gamma \equiv \frac{T_1 - T_4}{T_2 - T_3} = \frac{S_{14}}{S_{23}} \qquad (2.6)$$

The calculated S_{14} and S_{23} for T_o=400K is plotted in Fig. 5.
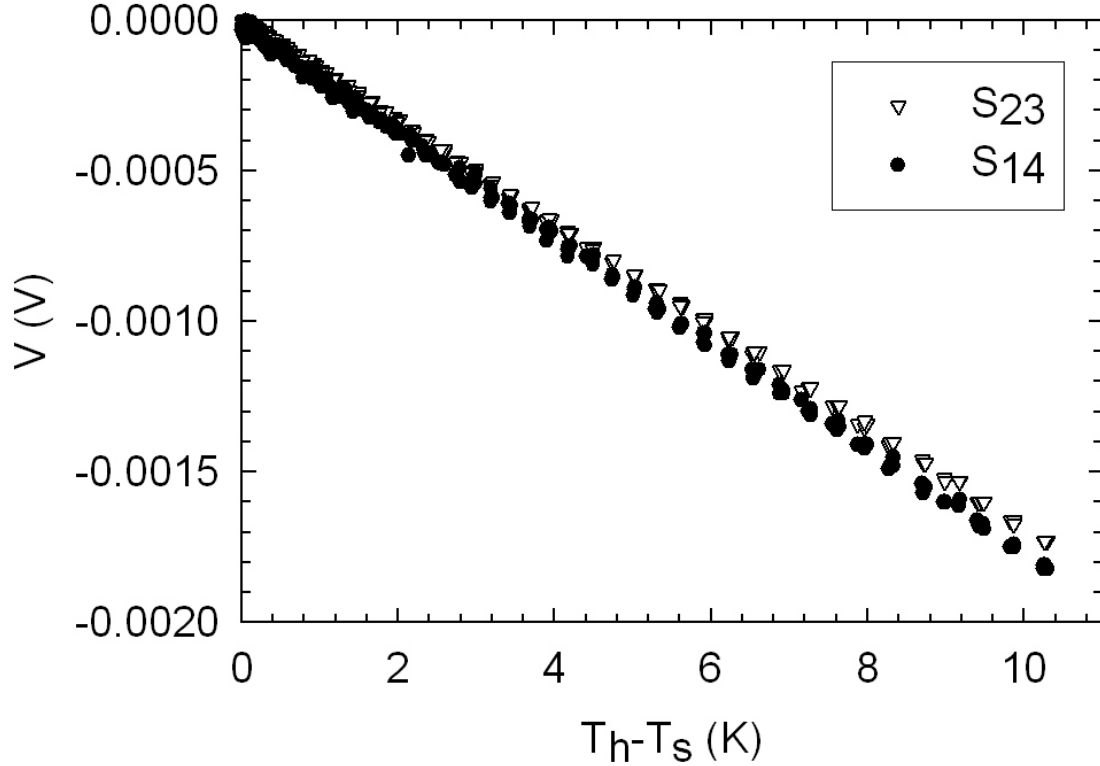
Fig. 5: Calculated S_{14} and S_{23} for T_o=400K across a $(PbSe_{0.99})_x(WSe_2)_x$ thin film. The difference in the thermoelectric voltage measured is due to the temperature drop across the sample because of the thermal contact resistance.

The γ value was used to obtain the total contact resistance $R_C = R_{C1} + R_{C2}$ and the sample thermal resistance R_s according to the following procedure.

Figure 2 illustrates heat transfer between the two membranes through the suspended nanofilm. Because the temperature of each nanofilm segment in contact with

the membrane varied along the length as a result of heat transfer between the nanofilm and the membrane, each nanofilm segment in contact with the membrane should be treated as a fin. The thermal contact resistance between the nanofilm and each membrane was thus the fin resistances, which was calculated using the fin resistance formula (Incropera 2007). The length scales used are illustrated in Fig. 6.

$$R_{C,i} = \frac{1}{\kappa A m \tanh(mL_{C,i})}; \quad i = 1 \text{ or } 2 \tag{2.7}$$

where κ and A are the thermal conductivity and cross section area of the nanofilm, $L_{C,i}$ is the length of the nanofilm segment in contact with one membrane, and m is defined as

$$m = \sqrt{\frac{hw}{\kappa A}} \tag{2.8}$$

where h is the thermal contact conductance per unit area between the nanofilm and the membrane, w is the width of the nanofilm.

The thermal resistance of the suspended segment of the nanofilm is

$$R_S = \frac{L_S}{\kappa A} \tag{2.9}$$

where L_S is the length of the suspended segment. According to the thermal resistance circuit in Fig. 2,

$$Q = \frac{T_h - T_h'}{R_{C,1}} = \frac{T_h' - T_s'}{R_S} = \frac{T_s' - T_s}{R_{C,2}} \tag{2.10}$$

According to the fin temperature profile

$$\frac{T_h - T_i}{T_h - T_h'} = \frac{\cosh(m(L_{C,1} - L_i))}{\cosh(mL_{C,1})}; \quad i = 1 \text{ or } 2 \tag{2.11a}$$

and

$$\frac{T_i - T_s}{T_s' - T_s} = \frac{\cosh(m(L_{C,2} - L_i))}{\cosh(mL_{C,2})}; \quad i = 3 \text{ or } 4 \tag{2.11b}$$

From the above equations, we obtained

$$\gamma_{14} \equiv \frac{T_1 - T_4}{T_h' - T_s'} = 1 + \frac{1 - \dfrac{\cosh(m(L_{C,1} - L_1))}{\cosh(mL_{C,1})}}{L_S m \tanh(mL_{C,1})} + \frac{1 - \dfrac{\cosh(m(L_{C,2} - L_4))}{\cosh(mL_{C,2})}}{L_S m \tanh(mL_{C,2})} \tag{2.12a}$$

$$\gamma_{23} \equiv \frac{T_2 - T_3}{T_h' - T_s'} = 1 + \frac{1 - \dfrac{\cosh(m(L_{C,1} - L_2))}{\cosh(mL_{C,1})}}{L_S m \tanh(mL_{C,1})} + \frac{1 - \dfrac{\cosh(m(L_{C,2} - L_3))}{\cosh(mL_{C,2})}}{L_S m \tanh(mL_{C,2})} \tag{2.12b}$$

$$\gamma = \frac{T_1 - T_4}{T_2 - T_3} = \frac{\gamma_{14}}{\gamma_{23}} \tag{2.12c}$$

and

$$\alpha = \frac{T_h - T_s}{T_h' - T_s'} = 1 + \frac{1}{L_S m}\left(\frac{1}{\tanh(mL_{C,1})} + \frac{1}{\tanh(mL_{C,2})}\right) \tag{2.13}$$

The parameter m was solved from Equation 12 and used to calculate α according to Equation 13 and γ_{23} according to Equation 12b. Matlab codes attached in appendixes A and B was used for calculating α and γ_{23}, and the following

$$S = \alpha S_{23} / \gamma_{23} \tag{2.14a}$$

$$G_s = \alpha G_{total} \quad \text{or} \quad R_s = R_{total} / \alpha \tag{2.14b}$$

$$R_C \equiv R_{C1} + R_{C2} = R_{total} - R_s = R_{total}(1 - 1/\alpha) \tag{2.14c}$$

The details of the uncertainty analysis of this four-probe measurement procedure are explained in appendix C.
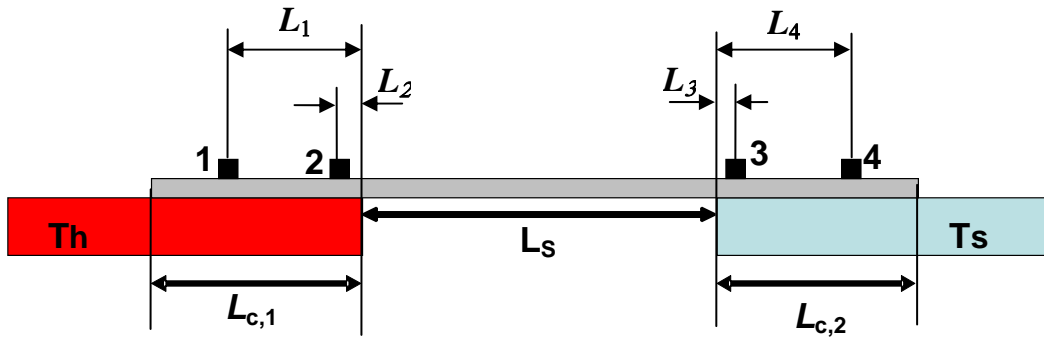
Fig. 6: Schematic of the suspended nanofilm indicating the length segments for the fin approximation.

Chapter 3: Combined Thermoelectric and Structural Characterization

of individual Bi$_{1-x}$Te$_x$ nanowires

The method described in Chapter 2 is used to measure the thermoelectric properties of individual Bi$_{1-x}$Te$_x$ nanowires and correlate the measured properties with the crystal structure characterized on the same nanowire with TEM. In addition, this chapter describes a method based on annealing the sample in a hydrogen environment to make electrical contact between the nanowire and the underlying Pt electrodes without using focused ion or electron beam induced deposition of metals.

3.1   Assembly of an individual Bi$_{1-x}$Te$_x$ nanowire on the measurement device

The Bi$_{1-x}$Te$_x$ nanowires were synthesized via electro-deposition into the nanopores of anodized alumina membranes (AAMs) by Jin et al. (Jin et al. 2004). The Bi to Te ratio was varied between different samples by varying the concentrations of the electrolytes. The AAM was dissolved in a NaOH solution and the obtained solution was rinsed with deionized water until a PH value of 7 was obtained. After the water was exchanged with isopropanol (IPA), a nanowire suspension in IPA was obtained.

A drop of the nanowire suspension was placed on a chip containing several microfabricated devices for thermoelectric measurements (Mavrokefalos et al. 2007). After the IPA evaporated, occasionally one Bi$_{1-x}$Te$_x$ nanowire was trapped between the two membranes of the suspended device and on top of the four pre-patterned Pt electrodes on the membrane, as illustrated in Fig. 7.
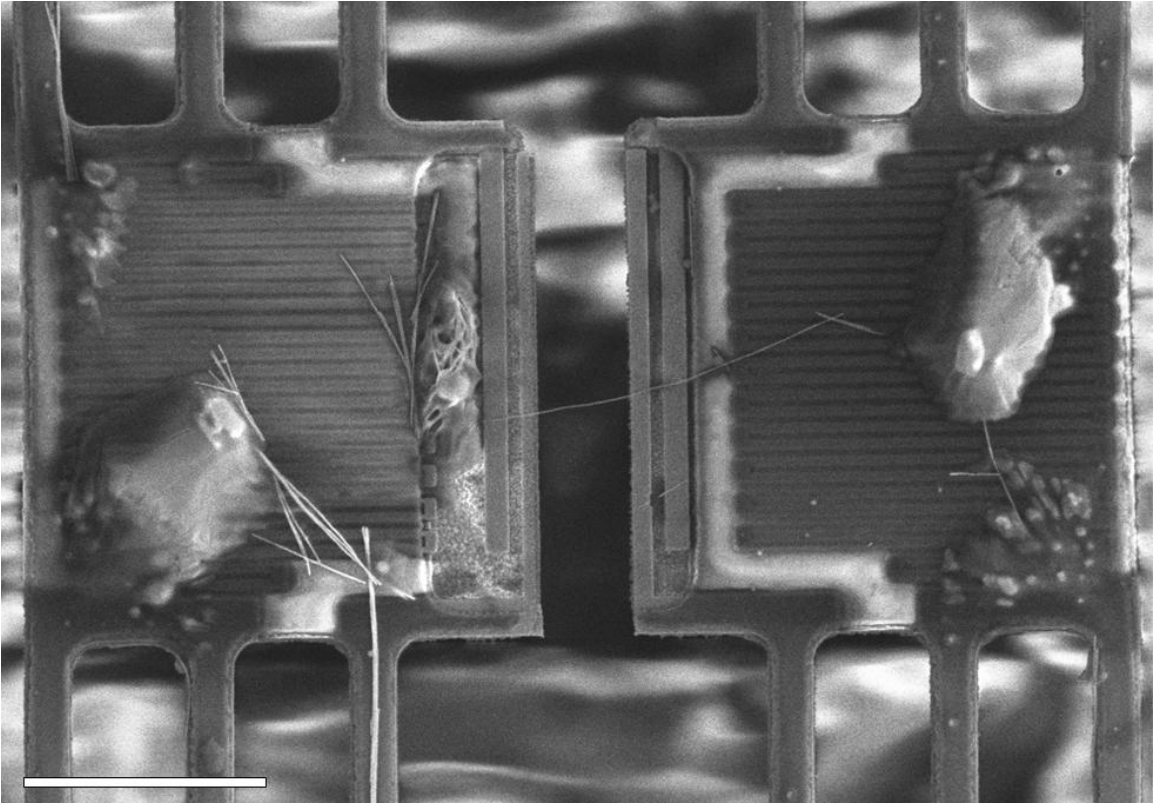
Fig. 7: Scanning electron microscopy (SEM) image of $Bi_{1-x}Te_x$ nanowire Sample 3 assembled between the two membranes of the suspended device. Scale bar is 10 μm.

3.2   Obtaining electrical contact to individual nanowires

The native oxide on the nanowire surface prevented electrical contact between the nanowire and the Pt electrodes. In previous works (Mavrokefalos et al. 2007, Mavrokefalos et al. 2007, Zhou et al. 2007, Zhou et al. 2005), focused ion beam induced metal deposition (IBIMD) or focused electron beam induced deposition (EBIMD) was used to deposit a small Pt pattern on top of the nanowire. The native oxide on the nanowire was damaged during the deposition process so that the electrical contact was made between the nanowire and the underlying Pt electrodes. It has been a concern that

24

the deposition process and especially the IBIMD process could damage or contaminate the nanowire sample.

To address the problem of making electrical contact to the nanowires without using the IBIMD or EBIMD Pt deposition process, in this work we have investigated another method based on *in situ* hydrogen annealing. After the sample was bonded to a ceramic chip carrier and the chip carrier was placed inside a continuous flow cryostat evacuated by a vacuum pump, forming gas containing five percent of hydrogen in nitrogen was introduced to the sample area when the sample stage temperature of the cryostat was raised to about 480 K. The flow rate of the forming gas was set to be about 5 standard cubic centimeters per minute (sccm). Ohmic contact between the $Bi_{1-x}Te_x$ nanowire and the four underlying electrodes could be obtained often within 20 minutes after the forming gas was introduced. Fig. 8 illustrates the two probe I-V curve probing the $Bi_{1-x}Te_{1x}$ nanowire for Sample 3 before and after annealing in forming gas. Before annealing there is no electrical contact between the nanowire and the electrodes and after the annealing there is a linear I-V curve.
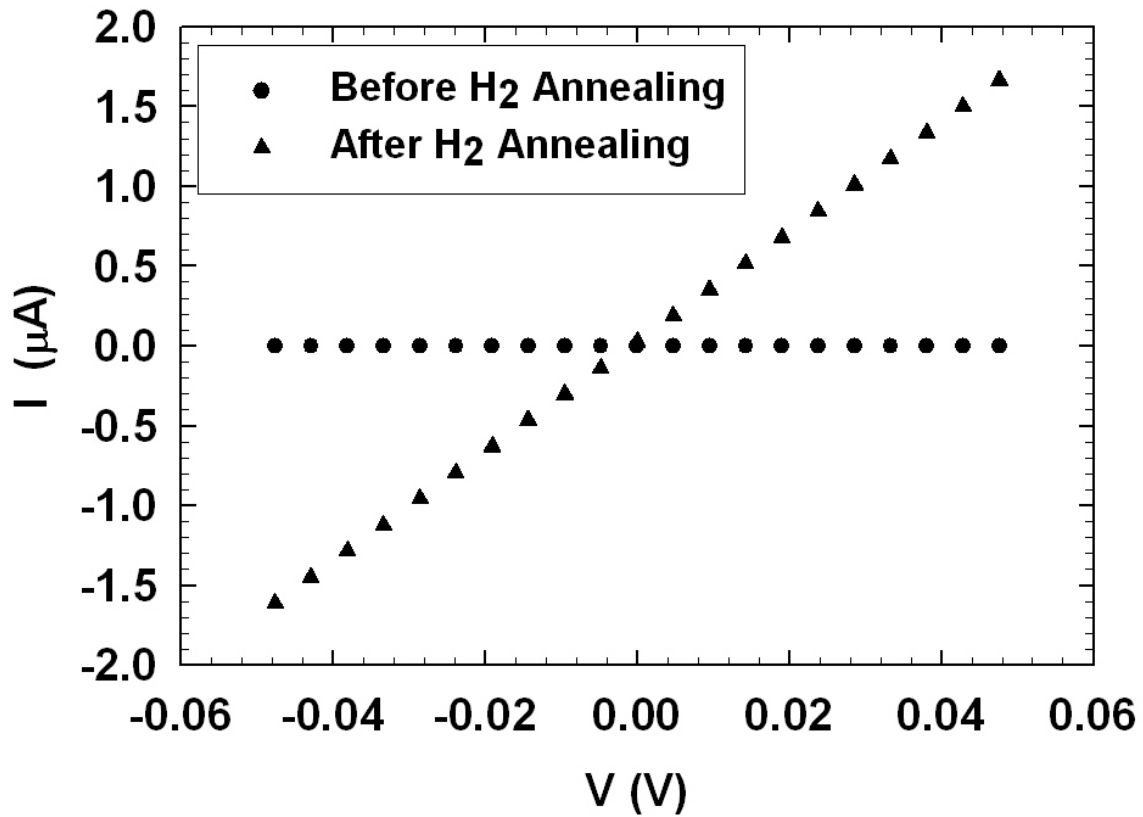
Fig. 8: The two probe I-V curve before and after annealing in forming gas environment for $Bi_{1-x}Te_x$ nanowire Sample 3.

3.3   Measurement Results and Discussions

The thermoelectric measurement was conducted following the four-probe measurement procedure as explained in Chapter 2 and reported recently (Mavrokefalos et al. 2007, Zhou et al. 2007). In this method, the nanowire-Pt junctions were used as thermocouple junctions to measure temperature drops at the contact so that the contact thermal resistance can be obtained. The electrical resistance was obtained by four-

terminal measurement (Fig. 9). Hence, both contact thermal and electrical resistances were eliminated in the obtained κ, S, σ, and ZT.
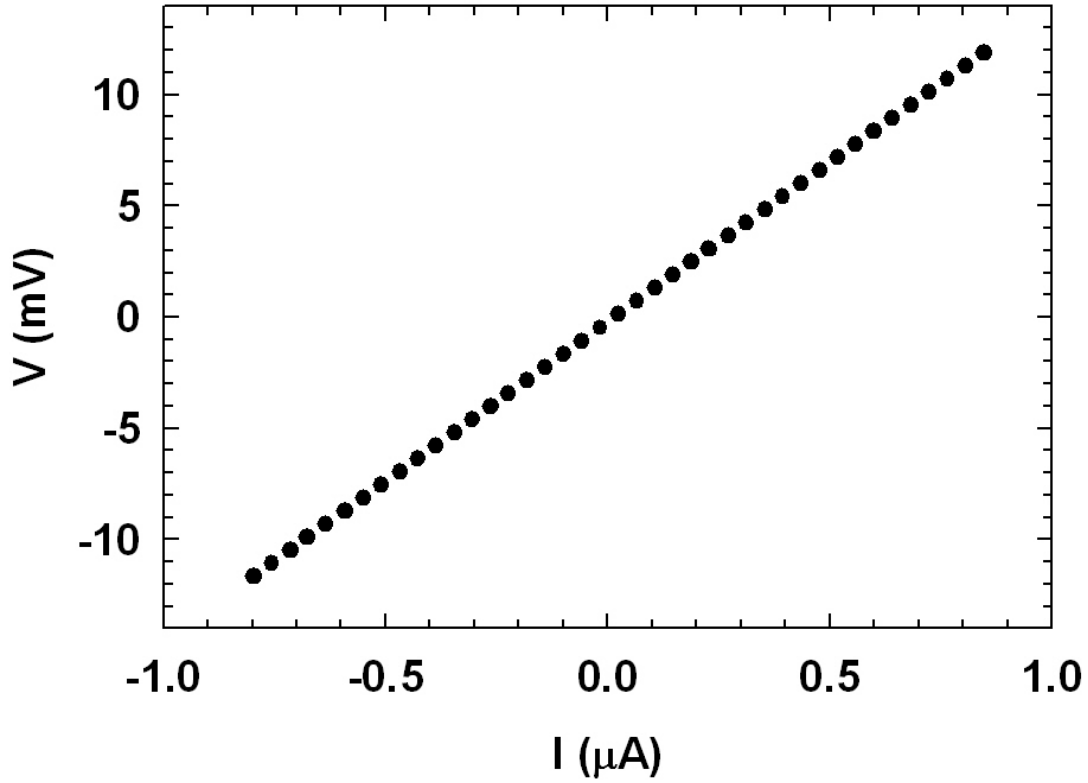
Fig. 9: Four-terminal resistance measurement of $Bi_{1-x}Te_x$ nanowire Sample 3 after annealing in forming gas environment for 30 minutes.

After the thermoelectric measurement, the sample was removed from the cryostat to a TEM for crystal structure characterization. A through-substrate hole under the suspended device allowed HRTEM of the nanowire assembled between the two suspended membranes. The HRTEM image in Fig. 10 reveals clear lattice fringes with a surface oxide thinner than 1 nm. This oxide thickness was much thinner than those observed previously on $Bi_{1-x}Te_x$ nanowires that were not annealed in the forming gas. The

very thin oxide on the annealed nanowire could have been formed when the sample was transferred in air from the cryostat to the TEM.
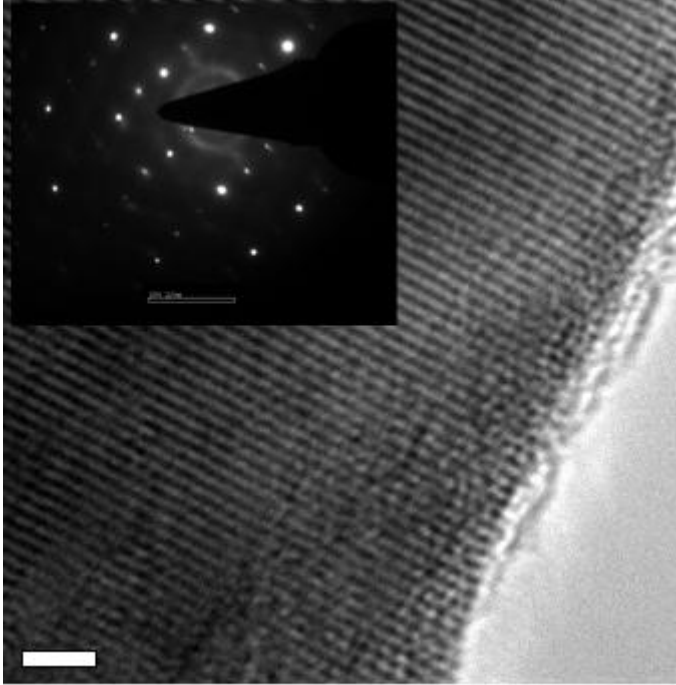
Fig. 10: HRTEM image of nanowire Sample 4 assembled on the device after hydrogen annealing and breaking the vacuum for transferring the sample from the cryostat to the TEM. The inset shows the selective area diffraction pattern. Scale bar is 2nm.

Thermoelectric measurements on four $Bi_{1-x}Te_x$ nanowires from different batches were conducted in this work. The targeted nanowire diameter was 60 nm and the measured diameter with TEM or scanning electron microscopy (SEM) was about 55 ± 2 nm for the three samples Sample 1 was broken during transfer from the cryostat to the TEM. Consequently, no TEM measurement results were obtained for this sample. Sample 4 is a nanowire from the same batch that only the 2 inner electrodes were in electrical

contact to the microdevice. Therefore only 2-probe thermal conductivity and Seebeck coefficient measurements were conducted for this sample. From the TEM image in Fig. 10, Sample 4 is of good crystalline quality and the crystal growth directions of these nanowires were found to be along $<11\bar{2}0>$ similar to that of Sample 3. TEM analysis was also carried out for Samples 2 and 3. The HRTEM image and the selective area electron diffraction (SAED) pattern in Fig. 11 suggest that Sample 3 is of good crystal quality with no significant defects or dislocations. The growth direction of this sample is determined from the SAED pattern to be along the $<11\bar{2}0>$ direction. On the other hand, the dark field TEM image of Sample 2 shows distinct grains along the nanowire length, as shown in Fig. 12. A dark field TEM of Sample 3 was not acquired but the bright field TEM shows no indication of any grain formation along the length of the nanowire. The atomic ratio was obtained using the energy dispersive spectrometer (EDS) of the TEM. EDS results for samples 1-4 revealed the same stoichiometry of 40% Bi and 60% Te. Because the EDS result on a single nanowire can have an uncertainty up to ±5%, the accuracy is insufficient to distinguish the different atomic ratios among different samples.
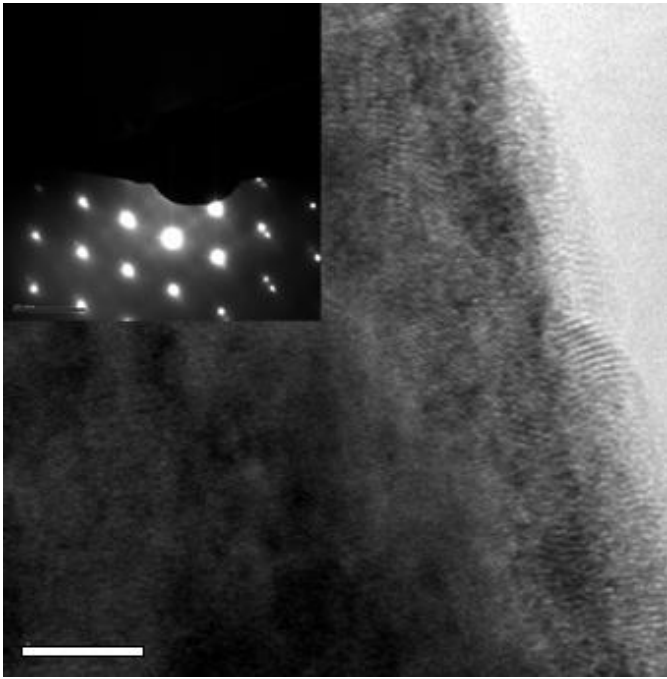
Fig. 11: HRTEM image of nanowire Sample 3 assembled on the device after hydrogen annealing and breaking the vacuum for transferring the sample from the cryostat to the TEM. The inset shows the selective area diffraction pattern. Scale bar is 5nm.
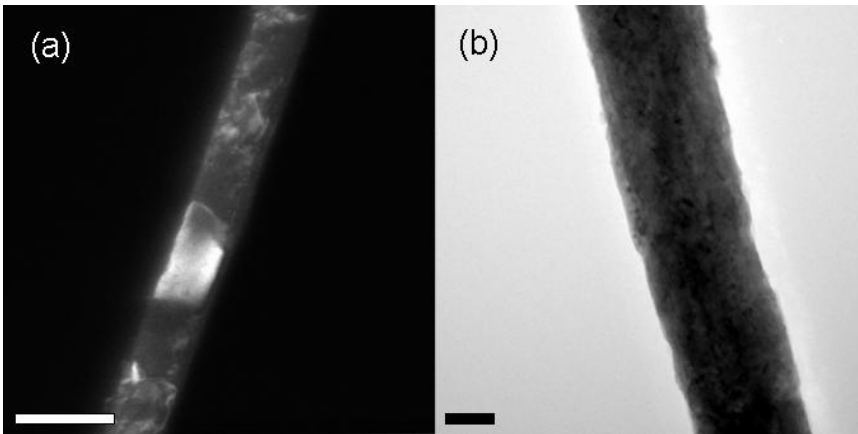
Fig. 12: (a) Dark field TEM image of Sample 2 showing distinct grains along the nanowire; (b) Bright field TEM image of Sample 3 showing no distinct grains along the nanowire. Scale bars are (a) 100 nm and (b) 20nm

Fig. 13(a) shows the Seebeck coefficient S as a function of temperature. All samples exhibit negative S that increases with T suggesting n-type doping. According to Fleurial et al. (Fleurial et al. 1988) the transition from p- to n- type in bulk $Bi_{1-x}Te_x$ compounds occurs at $n=10^{18}$ cm^{-3}. This transition in bulk depends on the atomic fraction of Te within the compound and corresponds to 62% atomic fraction of Te. Atomic fraction of Te smaller than 62% and electron concentration n smaller than 10^{18} cm^{-3} were found to lead to p-type doping; whereas Te atomic fraction larger than 62% and n larger than 10^{18} cm^{-3} leads to n-type doping. On the other hand, it has been reported that electrodeposited $Bi_{1-x}Te_x$ thin films (Yoo et al. 2005) exhibit n-type behavior at a Te concentration smaller than 62% because impurities in the film cause n larger than 10^{18} cm^{-3} at relative low Te content. Therefore, it is possible that impurities in the nanowires also cause an n-type behavior at a Te atomic fraction less than 62%. Moreover, the much lower Seebeck coefficient of the nanowires than the thin film suggests that the carrier concentrations in the nanowires are higher than that in the film.

Fig. 13(b) shows the electrical conductivity σ as a function of T. For all the samples, σ decreases with T, indicating that electron-phonon scattering is important. Samples 1 and 3 have similar σ, which is about 3 times higher than Sample 2 because of the much better crystal quality and less grain boundary scattering. The electrical conductivity of these two nanowire samples is also three times higher than that of the 6 μm thick film. (Fleurial et al. 1988)
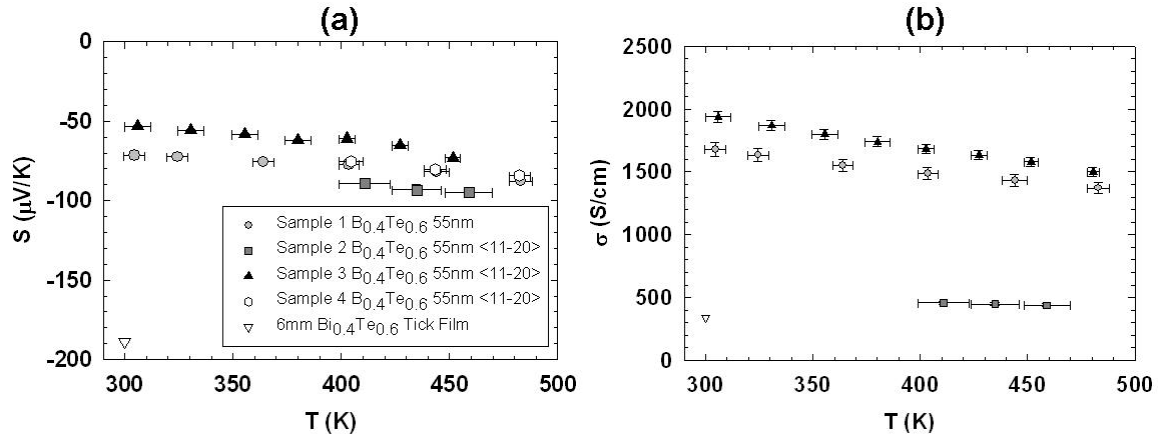
Fig. 13: (a) Measured *S* as a function of temperature for $Bi_{1-x}Te_x$ nanowires; (b) Measured *σ* as a function of T for $Bi_{1-x}Te_x$ nanowires. Also shown are the literature data on an electro-deposited 6 μm thick Bi_2Te_3 thin film. The two figures share the same legend shown in (a).

We have followed a procedure reported previously to extract the Fermi level from the measured Seebeck coefficient of the nanowires using the following equations (Seol et al. 2007, Zhou et al. 2007).

$$S = \frac{k_B}{e}\left\{\eta - \frac{[r_e + (5/2)]F_{r_e+3/2}}{[r_e + (3/2)]F_{r_e+1/2}}\right\}; \qquad \eta = \frac{E_F}{k_B T} \qquad (3.1)$$

where $F_m(n) = \int \xi^m d\xi /[e^{(\xi-\eta)} + 1]$ is the Fermi-Dirac integral of order *m*

Because the nanowires are degenerately doped, a single band model is used. Because electron-phonon scattering was found to be the dominant process, the electron scattering mean free time (τ) is assumed to depend on energy (E) according to $\tau \propto E^{r_e}$ where r_e=-0.5 (Ziman 1960). We note that electron-boundary scattering also leads

to $\tau \propto E^{-0.5}$ while electron-impurity scattering results in $\tau \propto E^{0.5}$ (Seol et al. 2007, Zhou et al. 2007). The extracted Fermi level shows an increasing trend with increasing temperature as expected in a semiconductor because of increased thermal activation of carriers with temperature (Fig. 14).
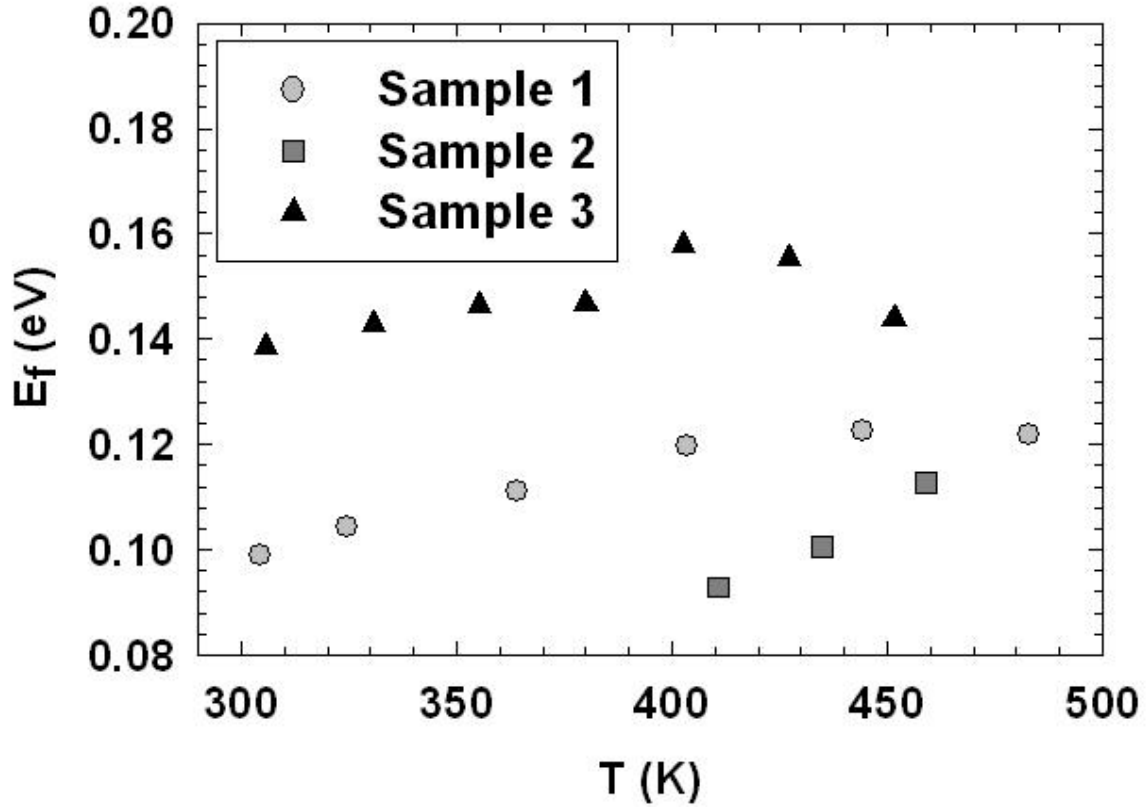
Fig. 14: Extracted Fermi level as a function of temperature for the nanowire samples.

With the extracted Fermi level, the carrier concentration was calculated using the following equation and electron effective mass of $m_e^*=0.271m_o$. This effective mass was averaged among the three principal directions for bulk $Bi_{1-x}Te_x$ (m_o is the electron mass)

$$n(T) = \frac{(2m_e^* k_B T)^{3/2}}{2\pi^2 h^3} F_{1/2} \qquad (3.2)$$

For the three samples, the carrier concentration is in the range between 2×10^{19} cm^{-3} and 4×10^{19} cm^{-3} (Fig 15(a)). The high electron concentrations suggest high donor impurity concentrations in the nanowires. However, the extracted carrier concentration was also found to increase with T suggesting that the intrinsic carriers account for an appreciable fraction of the total carrier concentration.

The electron mobility is further calculated based on the measured electrical conductivity and extracted carrier concentration according to $\mu = \sigma/ne$. As seen from Fig. 15(b), Samples 1 and 3 have a similar mobility that is much higher than that of Sample 2. The results suggest that grain boundary scattering reduces the mobility in Sample 2 that is polycrystalline and that Sample 1 could have a similar crystal quality as that of Sample 3. Even though the nanowires have similar mobility results to the n-type bulk (Fleurial et al. 1988), compared to the thin films (Yoo et al. 2005) the nanowire mobility results are 1 order of magnitude higher, potentially because the nanowires are of better crystalline quality than the granular electrodeposited thin films. Note that the thin film carrier concentration and mobility were obtained from the Hall measurement (Yoo et al. 2005).
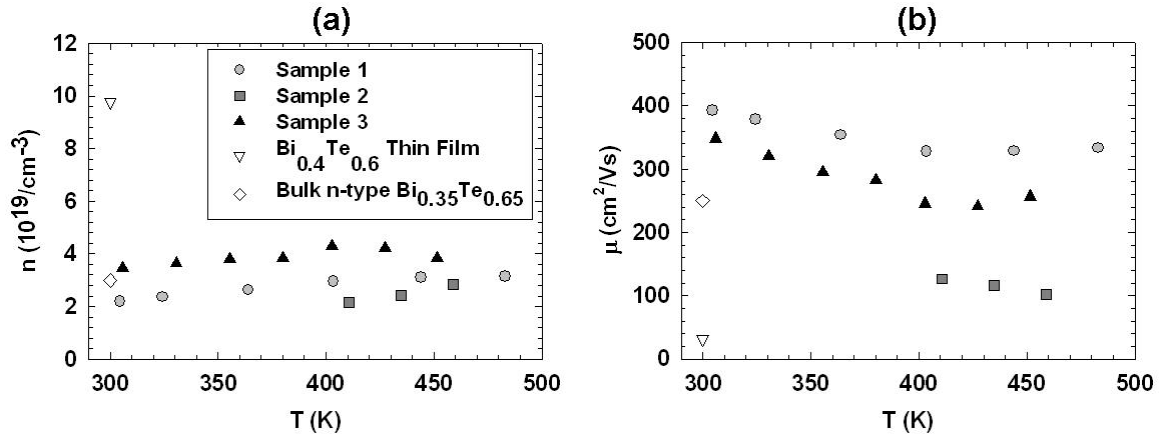
Fig. 15: Calculated carrier concentration (a), and mobility (b) as a function of temperature for the nanowire samples. The two figures share the same legend as shown in (a).

Figure 16(a) shows the measured two-probe conductance results. The two-probe thermal conductance of these nanowire samples was found to be quite low, between 1-3 nW/K, which is only a few times of the background conductance between the two membranes without a bridging nanowire. The background conductance is caused by residual air molecules in the evacuated cryostat, heating of the substrate, and radiation. To eliminate that error from our measurement we performed measurements on a blank microdevice to measure the background conductance and subtracted those from the two-probe thermal conductance (Fig. 16b). The corrected two-probe thermal conductance was used to calculate κ. The four-probe thermoelectric measurement technique was not used to calculate the thermal contact resistance and correct the κ, because the S values measured between the outer and inner electrodes did not reveal any significant difference, <2% difference. This indicates that the temperature drop along the nanowire length in contact with the microdevice was negligible.
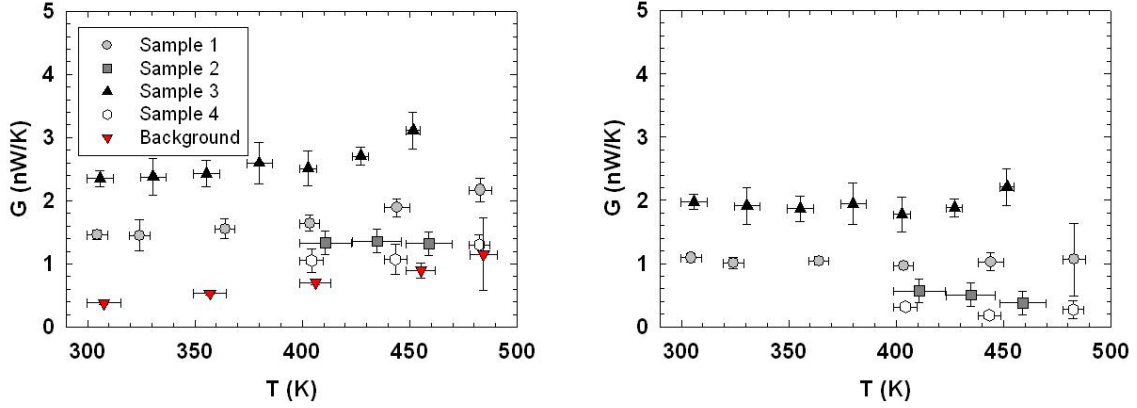
Fig. 16: (a) The measured thermal conductance of the four samples and the background thermal conductance (b) The corrected two-probe conductance of the four samples. The two figures share the same legend as shown in (a).

The thermal conductivity plotted in Fig. 17. The four samples have a κ value in the range of 0.4-3 W/m-K. In comparison, the thermal conductivity range between 1.8 and 3.3 W/m-K for n type and p type bulk $Bi_{1-x}Te_x$ crystals (Fleurial et al. 1988). Samples 1, 2 and 4 have κ values lower than the bulk. The suppressed κ in Sample 2 could be attributed to the presence of the grain boundaries along the length of the wire as illustrated in Fig. 12. The grain boundaries can scatter electrons and phonons and reduce κ. Sample 4 on the other hand is of good crystal quality with the growth direction perpendicular to the c axis. The κ suppression could thus be caused by surface scattering of energy carriers including phonons and electrons.

The lower κ of Sample 1 needs a careful analysis because the crystal structure of this sample was not characterized. This sample has the same value of S as Sample 4, which is from the same nanowire batch and is of good crystal quality. It also has just slightly lower electrical conductivity than Sample 3, which is also of good crystalline

quality. One possible phonon scattering mechanism for this sample is that of enhanced surface-phonon scattering (Chen et al. 2008, Hochbaum et al. 2008, Moore et al. 2008).

To better understand the measured thermal conductivity, we have calculated the electron contribution to the thermal conductivity (κ_e) of the nanowires 1-3 using the Wiedemann-Franz law. The Lorenz number in semiconductors depends on the carrier concentration, and deviate from that for a metal (Chen 2005). The Lorenz number used in the calculation is $L=1.5 \times 10^8$ WΩ/K^2, which is the value of bulk Bi$_2$Te$_3$. Figure 18(a) shows the obtained κ_e. The κ_e at about 400 K is between 0.8 – 1 W/m K for nanowire samples 1 and 3, and about 0.2 for nanowire 2 that has a lower n and poorer crystal quality than Sample 3. These values are all below the value of ~1.5 W/m K that is the maximum contribution of κ_e for n-type bulk Bi$_{1-x}$Te$_x$ when x value is 65% (Fleurial et al. 1988). The higher κ_e for Sample 3 can be attributed to the higher carrier concentration.

The difference between κ and κ_e is due to the lattice contribution (κ_l) and a bi-polar contribution (κ_{e-p}) caused by the thermal diffusion of electron-hole pairs that do not contribute to net charge transport or σ (Fig. 18(b)). The $\kappa_l + \kappa_{e-p}$ graph in the inset of Fig. 18(b) clearly shows a slightly increased $\kappa_l + \kappa_{e-p}$ with temperature at temperatured higher than 400 K for Samples 1 and 3, although we note that the variation could be within the uncertainty of the $\kappa_l + \kappa_{e-p}$ calculation. The bipolar contribution is known to increase the thermal conductivity as temperature increases. Moreover, for sample 2 that is polycrystalline, the calculated $\kappa_l + \kappa_{e-p}$ decreases with increasing temperature in the temperature range of 400-480 K, showing no signature of the bi-polar contribution.

The κ_l in bulk single $Bi_{1-x}Te_x$ crystals is ~1.7 W/mK at room temperature. The $\kappa_l +$ κ_{e-p} for both Samples 1 and 2 is lower than the bulk value, and that for Sample 3 is comparable to the bulk value. Moreover, while the σ and κ_e of Sample 1 are not much lower than those of Sample 3, it has much lower $\kappa_l + \kappa_{e-p}$ than Sample 3. However, the exact mechanism that leads to these different effects on σ and $\kappa_l + \kappa_{e-p}$ is unclear. Nevertheless, this finding that it is possible to suppress the $\kappa_l + \kappa_{e-p}$ term and also the κ_l, with much less reduction in the κ_e is intriguing and help to increase the ZT of Sample 1 to be higher than that of Sample 3, as show in Fig. 19.
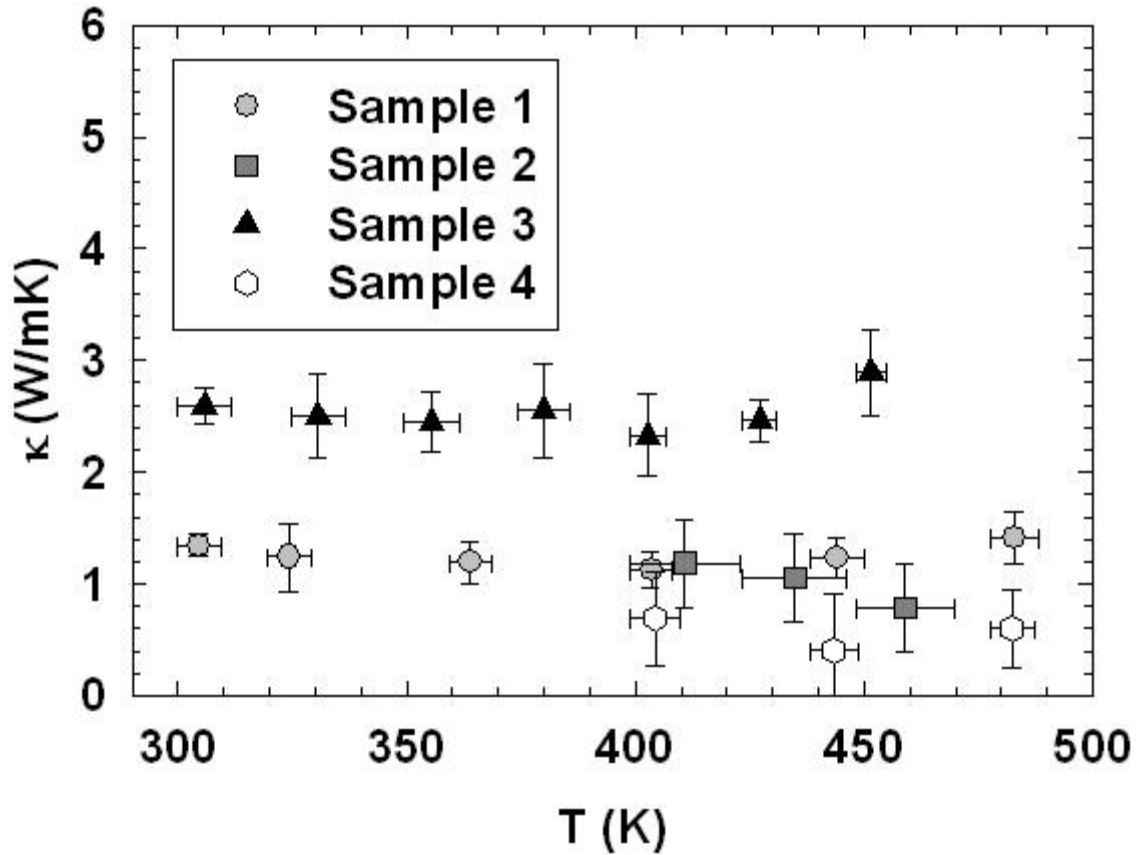
Fig. 17: Measured κ as a function of temperature for four Bi_2Te_3 nanowire samples.
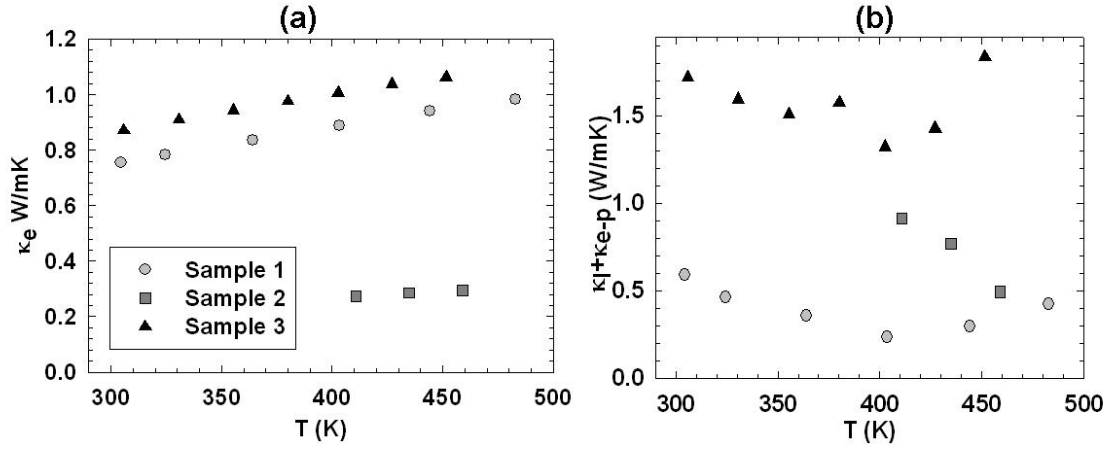
Fig. 18: (a) The calculated electron thermal conductivity (κ_e) as a function of temperature. (b) The calculated lattice and bi-polar thermal conductivity ($\kappa_l + \kappa_{e-p}$) as a function of temperature. The two figures share the same legend as shown in (a).

Figure 19 shows the calculated *ZT* for all the samples. Sample 1 has the highest *ZT* of ~0.3 at 500K whereas Samples 2 and 3 have similar values peaking at ~0.2 at 500K. The higher *ZT* for Sample 1 is due to the fact that of κ is suppressed below the bulk values probably due to the enhanced surface roughness phonon scattering without suppressing σ to a great extend. Samples 2 and 3 have similar *ZT* values but for different reasons. The bad quality of Sample 2 suppresses κ as well σ relative to the bulk keeping the overall *ZT* low. On the other hand the good crystal quality and smooth surface of Sample 3 preserves κ and σ within the bulk values. All 3 wires have *S* lower than bulk that keeps the overall *ZT* to low values. The reason for the low *S* is the high impurity or carrier concentration.
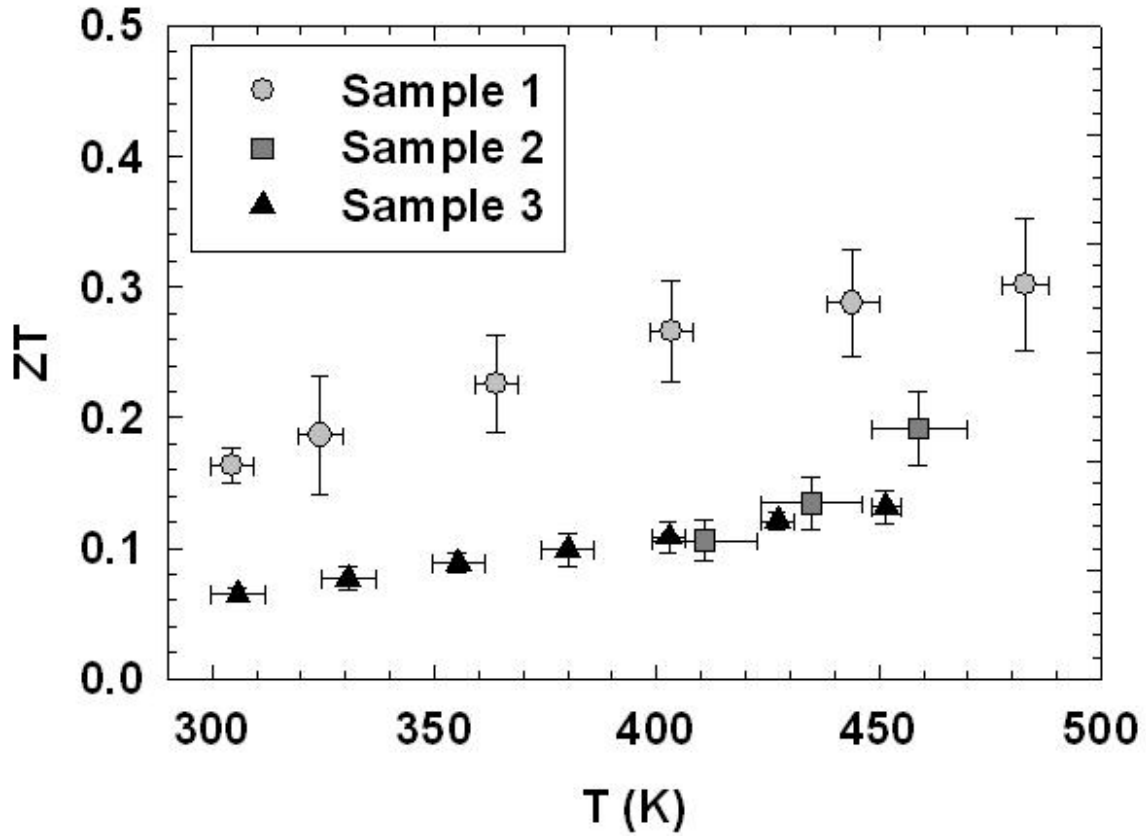
Fig. 19: Measured *ZT* as a function of temperature for three Bi_2Te_3 nanowire samples.

3.4   Summary

Thermoelectric measurements were performed on 4 individual $Bi_{1-x}Te_x$ nanowires of different stoichiometry. A new method of annealing the sample in forming gas environment was developed to make electrical contact between the sample and electrodes. The thermoelectric properties were found to be sensitive to the crystal quality and impurity doping concentration. All the wires were n-type with degenerately doped semiconducting behavior of decreasing σ with *T*. Nanowires of better crystalline quality had higher κ, and σ. Samples with good crystal quality both exhibited the highest and

lowest κ. Only 1 sample had κ comparable to that of bulk $Bi_{1-x}Te_x$. The other 3 samples exhibited lower electronic and lattice contribution to the thermal conductivity probably because of enhanced grain boundary and surface phonon scattering. The highest *ZT* value was 0.3 at a temperature of 500K. It has been shown that κ can be suppressed beyond the bulk values either from grain boundary or enhanced surface roughness boundary scattering. The lower *ZT* found in the nanowires is attributed to the high impurity or carrier concentration and defects in the nanowires. Furthermore potentially an enhancement in *ZT* can be realized through suppression of κ without negatively affecting σ.

Chapter 4: Characterizations of the In-Plane Thermoelectric Properties of Disordered, Layered Thin Films

This chapter describes an application of the method discussed in Chapter 2 for the characterization of the in-plane thermal and thermoelectric properties of disordered, layered thin films grown by Johnson et al. using the Modulated Elemental Reactant Techniques (MERT) (Heideman et al. 2008). Three types of films were characterized, namely WSe_2, $W_x(WSe_2)_y$ and $[(PbSe)_{0.99}]_x(WSe_2)_x$. These films are polycrystalline within each layer, with mis-oriented adjacent layers. The cross-plane thermal conductivity of these films was measured by Cahill et al. using the time domain thermal reflectance (TDTR) method and found to be much lower than the thermal conductivity of the amorphous phase, and approach two times of the thermal conductivity of air at room temperature (Chiritescu et al. 2007). The thermal property of the film is expected to be very anisotropic. However, the TDTR method is not capable of measuring the in-plane thermal conductivity of the film. Here, the in-plane thermal conductivity is measured using the suspended device. For the $[(PbSe)_{0.99}]_x(WSe_2)_x$ film, the in-plane Seebeck coefficient and electrical conductivity are measured together with the in-plane thermal conductivity on the same sample. The in-plane measurement result may help to explain the extremely low thermal conductivity in the cross-plane direction.

4.1 WSe$_2$ and W$_x$(WSe$_2$)$_y$ superlattice thin films

4.1.1 Sample preparation and structure characterization

The superlattice thin films were grown by Johnson et al. using the Modulated Elemental Reactant Technique (Noh et al. 1996). During the growth process, the elements were sequentially deposited in a high vacuum chamber (1x10^{-7} Torr background pressure) onto unheated pre-polished Si wafer (roughness ±3Å). Elemental W (99.95% purity) was deposited at 0.2Å/s using 3kW electron beam guns while Se (99.995% purity) was delivered using a Knudsen effusion cell depositing at 0.5Å/s. A computer program controlled the thicknesses of the elements deposited, opening a shutter for either a specified period of time or responding to the integrated thickness signal of quartz crystal monitor. To make $[(W)_x(WSe_2)_y]_z$ superlattice, y sequences of WSe$_2$ reactants were deposited followed by a thick layer of W reactant to make x unit cells of W. The process was repeated z number of times to make the final superlattice. For this sample 4 unit cells of W and 10 unit cells of WSe$_2$ were deposited 24 times to produce a superlattice film with total thickness of about 190nm, as shown in Fig. 20. Electron Probe Micro Analysis and Rutherford Back Scattering measurements show that the repeat thickness of the W$_4$(WSe$_2$)$_{10}$ layer is 83.6±0.1 Angstroms. The calibration part of the WSe$_2$ block gives a W:Se ratio of 0.93-0.95:2
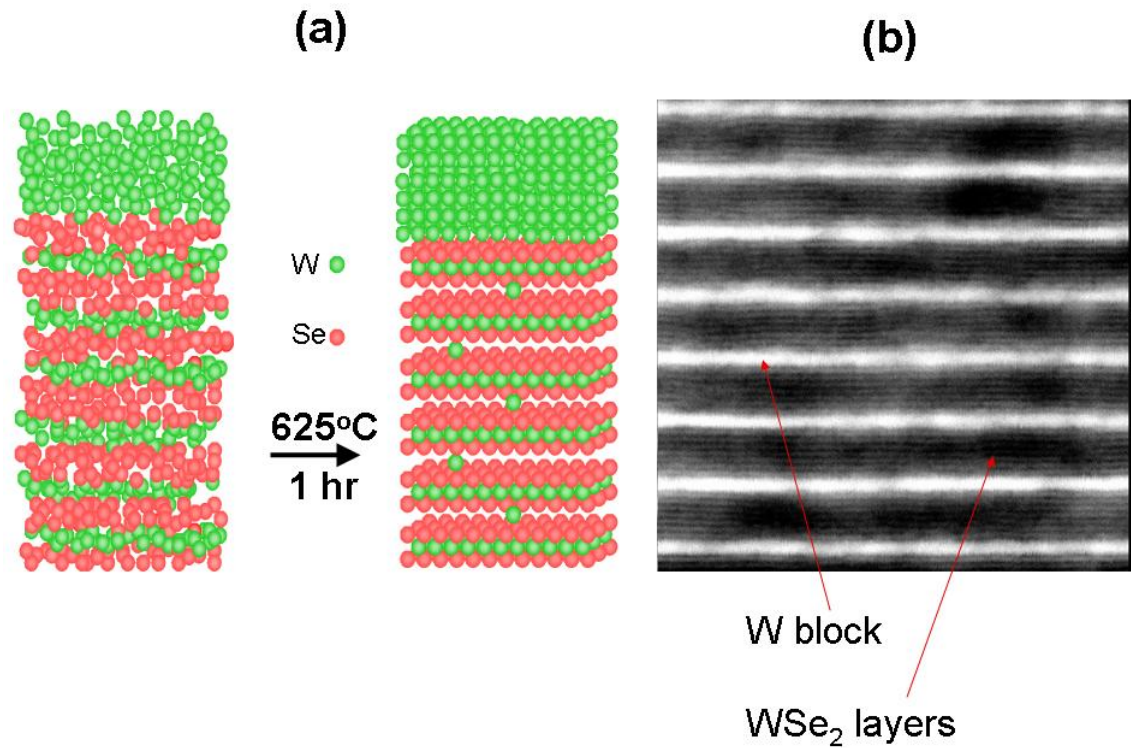
Fig. 20: (a) A schematic showing the designed reactants to produce $(W)_4(WSe_2)_{10}$ superlattice, (b) Transmission Electron Microscopy image of the superlattice film.

To perform the TE measurements, individual thin films were patterned as illustrated in Fig. 21. EBL was used to pattern arrays of ZEP-520 resist lines of different widths ranging from 0.5 to 2 μm and lengths ranging from 10 to 15μm. This resist pattern was used as an etching mask to etch through the film using a Reactive Ion Etcher (RIE) with CHF_3 chemistry (40sccm, 40mTorr, 150W). After the pattern was transferred to the film, the residual resist was stripped using oxygen plasma etching

44
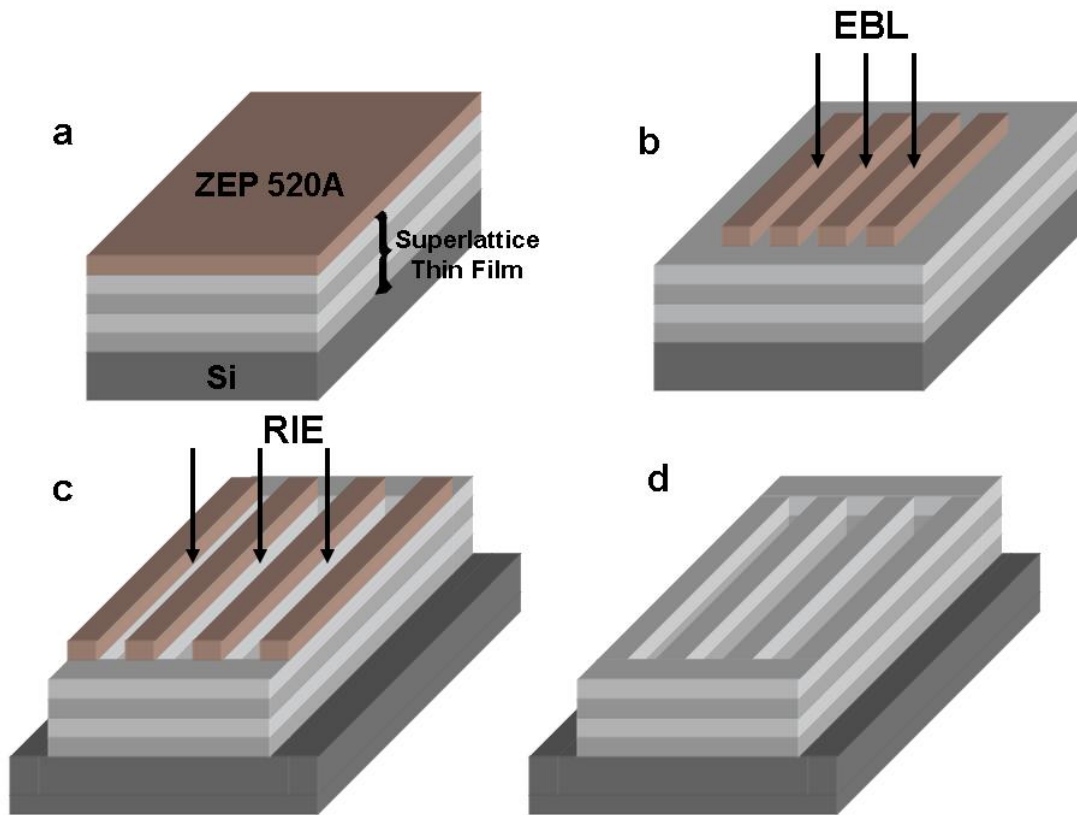
Fig. 21: Fabrication process to pattern individual WSe_2 and $W_x(WSe_2)_y$ individual thin film segments.

The thin films were transferred to the suspended micro-device using a Zyvex S100 Nanomanipulator System. This system uses a sharp tungsten tip actuated by a nanometer resolution piezoelectric transducer in a Scanning Electron Microscope (SEM). Because the adhesion between the film and the silicon substrate is very poor, the film could be peeled off by the tip and transferred directly to the suspended micro-device as illustrated in Fig. 22. To enhance the electrical as well as the thermal contact to the micro-device we used Electron Beam Induced Metal Deposition (EBIMD) to deposit a

250 nm wide, 150 nm thick, 2 μm long Pt line on top of the thin film and each of the four

underlying Pt electrodes pre-patterned on the suspended device, as illustrated in Fig. 23.
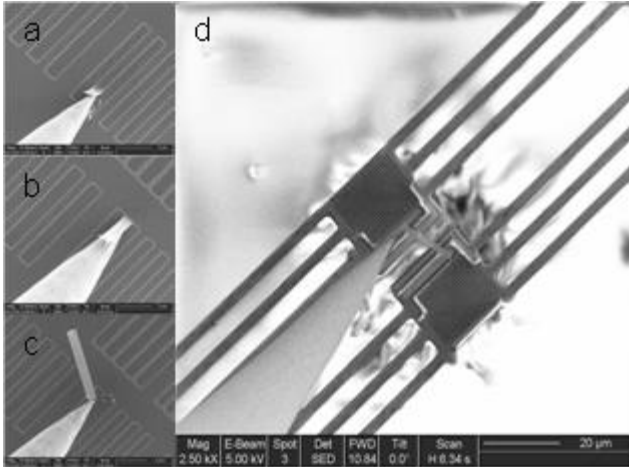
Fig. 22: Transfer of patterned thin film to the micro-device using the nanomanipulator

system
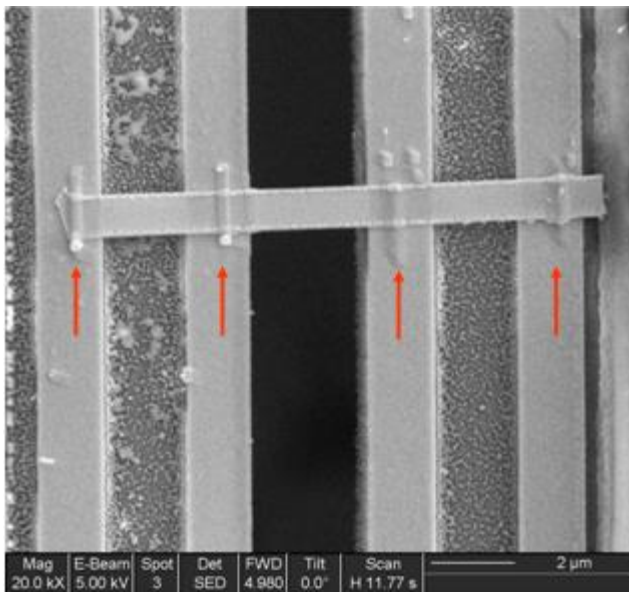
Fig 23: SEM of an assembled patterned $(W)_4(WSe_2)_{10}$ thin film. The arrows indicate the

four Pt depositions on top of the contacts between the thin film and the electrodes.

After the film was assembled on the micro-device and the TE measurements were performed, the etched edge of one suspended $W_4(WSe_2)_{10}$ film was analyzed using High Resolution Transition Electron Microscopy (HRTEM), which showed moiré fringes indicative of slightly mis-oriented crystal layers throughout the sample (Fig. 24). Tungsten (110) lattice fringes were prominent in the bright field images and it is most likely that these thick W layers are responsible for the linear moiré patterns. Selected Area Diffraction (SAD) revealed the polycrystalline nature of the superlattice showing a discrete number of comparatively large W grains within the illuminated area. The inter-planar spacings of both W and WSe_2 were within 0.5% of those reported for bulk W and WSe_2 by x-ray powder diffraction. Additionally, SAD showed only [*hk0*] reflections from the WSe_2 layer, indicating the [0001] axis perpendicular to the transport direction for the in-plane measurement as expected.
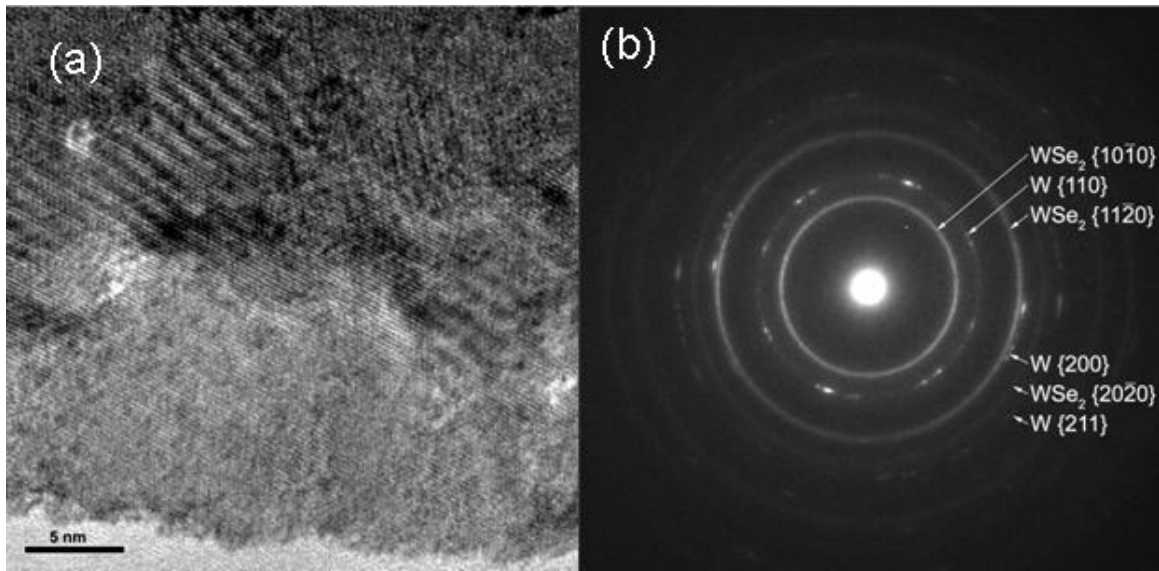
Fig. 24: (a) Top-view HRTEM of the etched edge of a suspended $(W)_4(WSe_2)_{10}$ film assembled on the micro-device. (b) The Selected Area Diffraction pattern.

4.1.2   Thermoelectric Characterization

After the sample was bonded on a ceramic chip carrier, the chip carrier was placed in a continuous flow cryostat evacuated by a vacuum pump at a base pressure less than 10^{-6} torr. The measured TE properties of the $[W_x(WSe_2)_y]_z$ and WSe_2 thin films that are listed in Table 4.1 are illustrated in Fig. 25 and 26. Because these samples either have low Seebeck coefficient or low electrical conductivity, the four-probe thermoelectric measurement technique could not be used here to obtain the contact temperature drops. Therefore the results plotted here are those of the two-probe thermal conductivity. Based on previous results (Mavrokefalos et al. 2007, Zhou et al. 2007) the contact thermal resistance can be between 10%-30%.

Table 4.1. Compositions and dimensions of the WSe_2 and $W_x(WSe_2)_y$ thin film samples.

Sample #	1	2	3	4
Composition	WSe_2	WSe_2	$W_4(WSe_2)_{10}$	$W_4(WSe_2)_{10}$
Thickness (nm)	162	162	140	140
Width (nm)	1633	1639	951	1499
Length (nm)	6074	4762	2935	4955

As shown in Fig. 25 the obtained in-plane κ results at room temperature are in the range of $1.2 - 1.6$ W m^{-1} K^{-1} , which is about 30 times higher than the cross-plane κ obtained by the Cahill group using the TDTR method on WSe_2 and $W_x(WSe_2)_y$ thin film samples synthesized under the same condition (Chiritescu et al. 2007). The anisotropy ratio is much higher than that of compacted single-crystal horizontal WSe_2 platelets, which has an in-plane κ of 9.7 W m^{-1} K^{-1} and cross-plane κ of 2.09 W m^{-1} K^{-1}. The increased κ anisotropy verifies the in-planed ordered and cross-plane disordered nature of the rotationally disordered layered structure of the films. It may also explain the extremely low cross-plane thermal conductivity. Because of the in-plane ordered, cross-plan disordered structure, phonons are scattered by the interface between adjacent layers into predominately along the in-plane direction, leading to an extremely low cross-plane thermal conductivity and a much higher high-plane thermal conductivity.

However, the in-plane κ is still about six times lower than that of the compacted single-crystal platelets. The lower in-plane values in the disordered films could be caused by smaller lateral grain size (about 6-10 nm from both diffraction and TEM

measurements), which is evident in the two times lower in-plane electrical conductivity (0.014 Ω^{-1} cm^{-1}) in WSe_2 thin film sample 2 than in the compacted single-crystal WSe_2 platelets. However, the in-plane κ reduction could also be caused by increased scattering of the in-plane phonon modes by the boundaries between adjacent layers in the disordered films than in the single crystal.
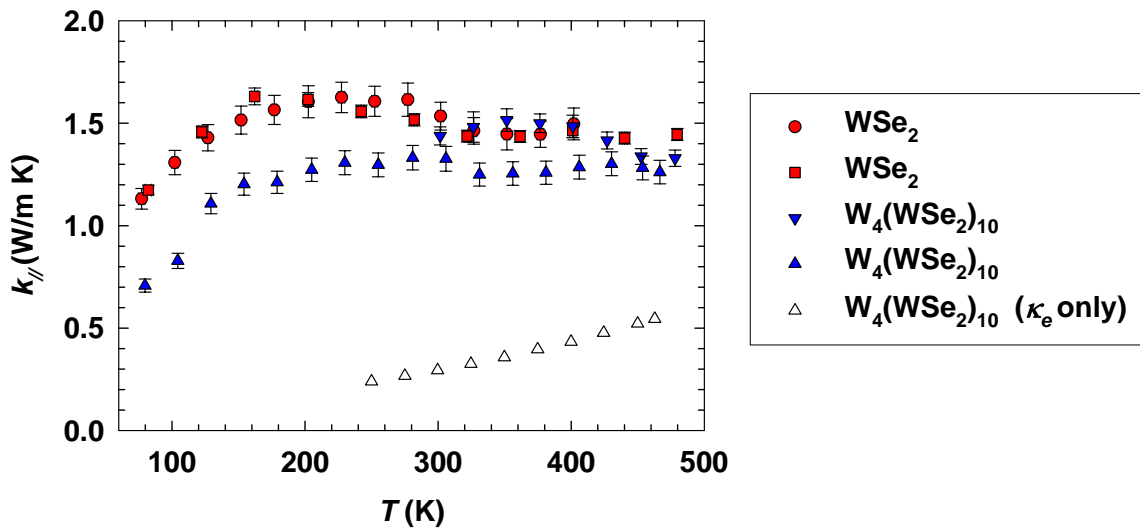
Fig. 25: Measured thermal conductivity of the four WSe_2 based thin film samples.

The obtained in-plane σ, S and ZT for the $[W_4(WSe_2)_{10}]_{24}$ are shown in Fig. 26 as a function of temperature. The Seebeck coefficient reported in the figure was the relative value to that of the thin film Pt electrodes. We note that the reported Seebeck coefficient for commercial thermocouple elements are usually the relative Seebeck coefficient measured against bulk Pt electrodes, which has a small Seebeck coefficient of -5.28 μV/K at room temperature (Rowe 1995). The Seebeck coefficient of the thin film Pt electrodes is expected to be small. Hence, the absolute Seebeck coefficient of the

superlattice film sample should be small, as expected for a metal. Because of the large electrical resistance of the WSe_2 sample, S could not be measured.

The in-plane electrical conductivity for the $[W_4(WSe_2)_{10}]_{24}$ film was found to be in the order of 400 S/cm. This value is much higher than the value of 0.014 S/cm we measured for pure WSe_2 thin films grown by the same method. This increase in electrical conductivity can be attributed to the additional W blocks added to the superlattice thin film. For sample 4, the electron contribution (κ_e) to κ can be estimated from the measured electrical conductivity according to the Widemann-Franz law, with the Lorenz number being 2.45×10^{-8}. As shown in Fig. 25, κ_e is about one-third of the measured total κ for sample 4 at room temperature. Hence, κ_l contributes to about two-thirds of the total κ of sample 4. Not shown in Fig. 25, the estimated κ_e is about five orders of magnitude lower than the total κ of sample 2 so that κ_l of the WSe_2 sample is essentially the same as the measured total κ. Comparing the deduced κ_l results of the WSe_2 film and the $[W_4(WSe_2)_{10}]_{24}$ film, one can note that the addition of W layers in the $[W_4(WSe_2)_{10}]_{24}$ film reduce its in-plane κ_l for about 30 percent compared to the WSe_2 film.
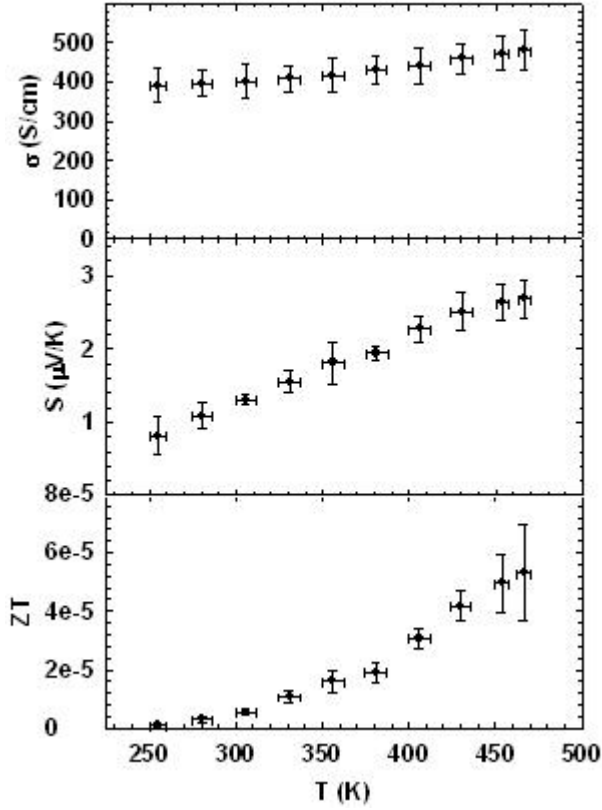
Fig. 26: Measured electrical conductivity σ, Seebeck coefficient S, and ZT of a $[W_4(WSe_2)_{10}]_{24}$ thin film.

4.2 $[(PbSe)_{0.99}]_x(WSe_2)_x$ Superlattice Thin Films

4.2.1   Sample preparation and structure characterization

The $[(PbSe)_{0.99}]_x(WSe_2)_x$ Superlattice Thin Films were grown by Johnson et al. using the MERT method. The misfit layered compounds $[(PbSe)_{0.99}]_x(WSe_2)_x$ were self-assembled from designed precursors prepared by sequentially depositing m bilayers containing Pb and Se in a 1:1 atomic ratio followed by n bilayers containing W and Se in a 1:2 ratio. In each bilayer, the ratio of the layer thicknesses was adjusted to obtain the

composition corresponding to the stoichiometry of the desired component compound and the absolute thickness of each bilayer was adjusted to provide the number of atoms required to form a Pb-Se rock salt bilayer or Se-W-Se trilayer. The thin films were grown on top of a Si substrate.

Individual $[(PbSe)_{0.99}]_x(WSe_2)_x$ superlattice thin films were patterned in a way similar to that for the WSe_2 superlattice thin films as illustrated in Fig. 27. A 300nm thick SiO_2 film was grown using Plasma Enhanced Chemical Vapor Deposition (PECVD) on top of the $[(PbSe)_{0.99}]_x(WSe_2)_x$ thin film to use as an etching mask to etch the $[(PbSe)_{0.99}]_x(WSe_2)_x$ thin films. The reason the SiO_2 was chosen as an etching mask was because no suitable chemistry was found to etch the $[(PbSe)_{0.99}]_x(WSe_2)_x$ film via RIE. Therefore physical Ar ion sputtering was used to etch the film, making it necessary to use SiO_2 as the etching mask. After the SiO_2 deposition, EBL was used to pattern arrays of ZEP-520 resist lines of different widths ranging from 0.5 to 5 μm and lengths ranging from 20 to 35μm. This resist pattern was used as an etching mask to etch through the SiO_2 film using a RIE with CHF_3 chemistry (25sccm CHF_3, 5sccm O_2, 50mTorr, 150W). After the pattern was transferred to the SiO_2 film the pattern was transfer to the $[(PbSe)_{0.99}]_x(WSe_2)_x$ film using Ar sputtering (80sccm Ar, 50mtorr, 250W). There was no need to strip any residual ZEP-520 resist because the time that is needed for the pattern to transfer to the $[(PbSe)_{0.99}]_x(WSe_2)_x$ film, the polymer is completely removed. The remaining SiO_2 film is removed by dipping the sample in a solution of Buffered Oxide Etch (BOE).
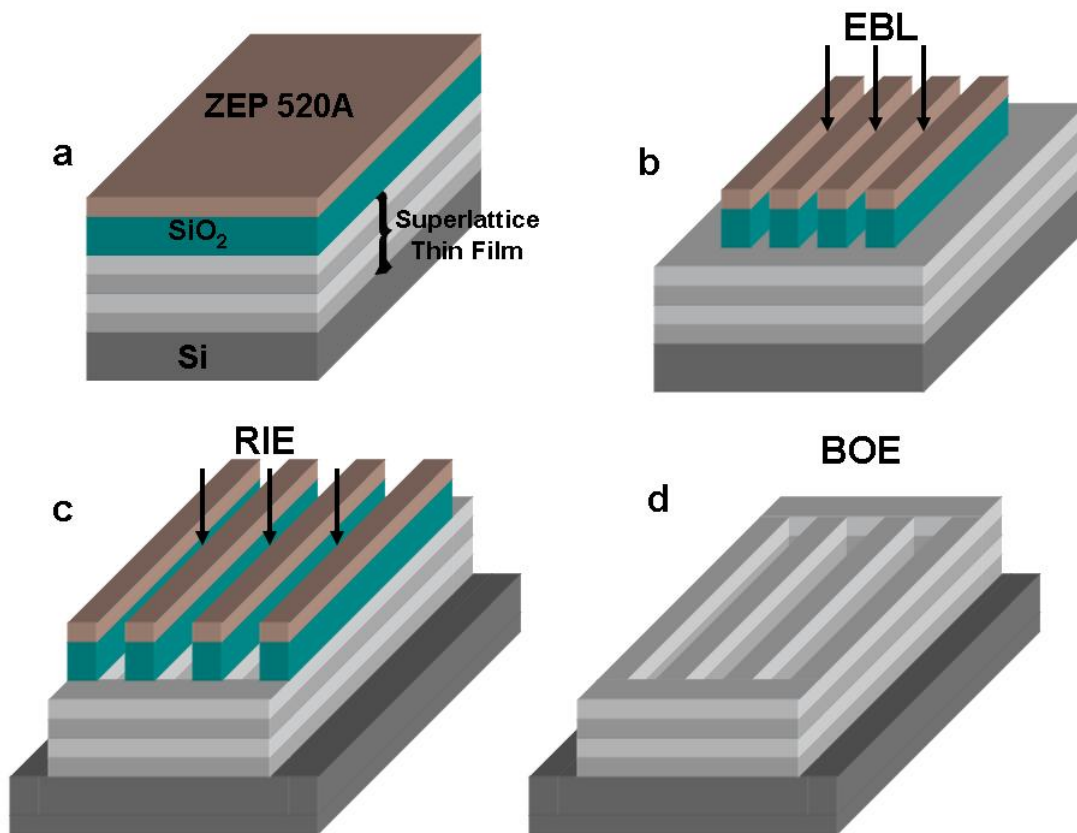
Fig. 27: Fabrication process to pattern individual $[(PbSe)_{0.99}]_x(WSe_2)_x$ thin film segments

The individual thin film segments were transferred onto the microdevice using the Zyvex S-100 nanomanipulator in the same manner as explained previously. Small amounts of Pt were deposited using EBIMD to enhance the electrical end thermal contact. Fig. 28 shows a thin film segment of $[(PbSe)_{0.99}]_x(WSe_2)_x$ suspended on the microdevice. The arrows show the Pt patterns deposited using EBIMD.
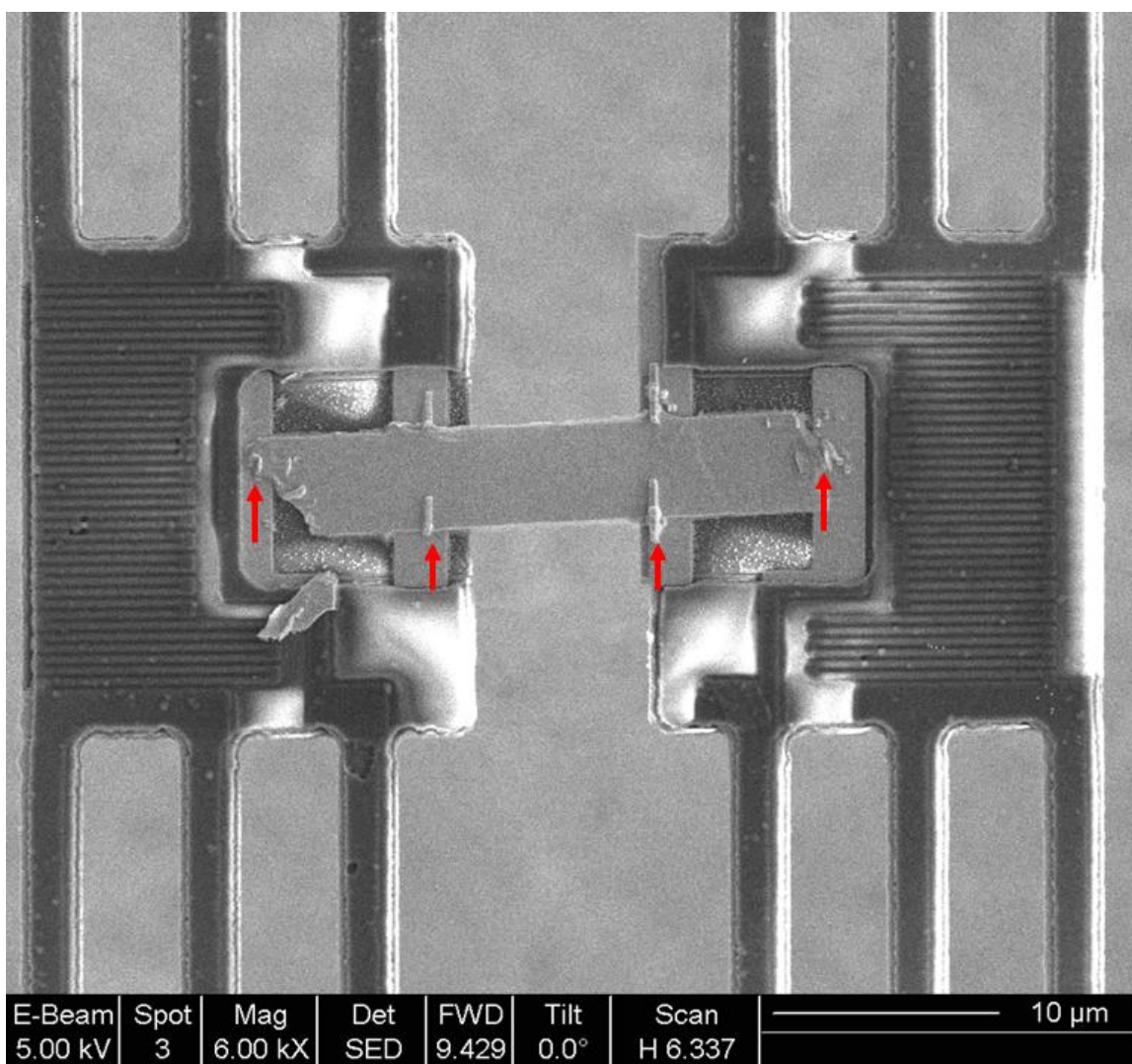
Fig. 28: SEM of an assembled patterned $[(PbSe)_{0.99}]_x(WSe_2)_x$ thin film. The red arrows indicate the four Pt depositions on top of the contacts between the thin film and the electrodes.

After the film was assembled on the micro-device and the thermoelectric measurements were performed, the etched edge of the suspended $[(PbSe)_{0.99}]_4(WSe_2)_4$ film was analyzed using High Resolution Transition Electron Microscopy (HRTEM), which showed moiré fringes indicative of slightly miss-oriented crystal layers throughout

the sample (Fig. 29) validating the mis-oriented structure similar to the $[W_4(WSe_2)_{10}]_{24}$ superlattice films. Diffraction analysis was inconclusive for this sample because the sample was too thick (152 nm) and the device could not reach the eutectic focal plane of the TEM.
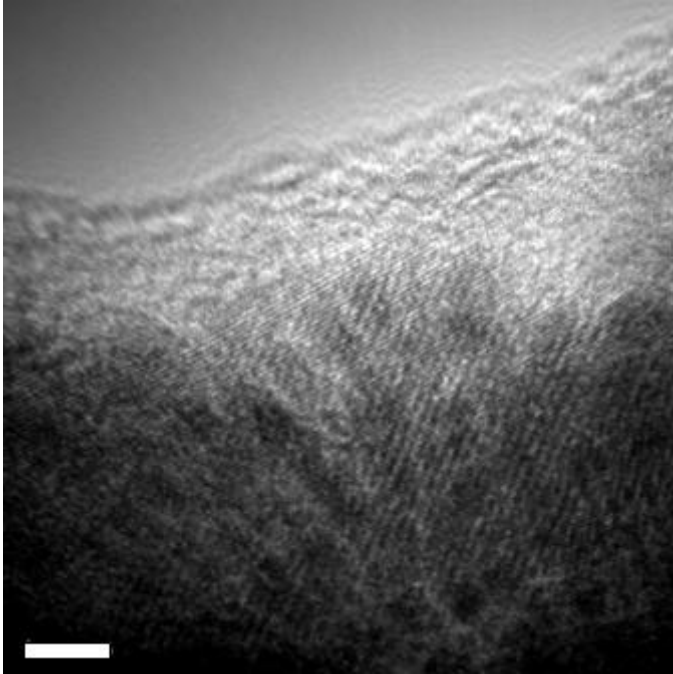
Fig. 29: Top-view HRTEM of the etched edge of a suspended $[(PbSe)_{0.99}]_4(WSe_2)_4$ film assembled on the micro-device. Scale bar is 5 nm.

4.2.2 Thermoelectric Characterization

After the sample was bonded on a ceramic chip carrier, the chip carrier was placed in a continuous flow cryostat evacuated by a vacuum pump at a base pressure less than 10^{-6} torr. Thermoelectric properties of the four $[(PbSe)_{0.99}]_x(WSe_2)_x$ thin films listed in Table 4.2 were measured. The results are shown in Fig. 30-31. The four samples have different unit cell size with varied numbers of layers of PbSe and WSe$_2$ in the unit cell.

[(PbSe)$_{0.99}$]$_2$(WSe$_2$)$_2$, [(PbSe)$_{0.99}$]$_3$(WSe$_2$)$_3$, and [(PbSe)$_{0.99}$]$_4$(WSe$_2$)$_4$ have 2 x 12.7Å, 3 x 12.7Å, 4 x 12.7 Å unit cell sizes, respectively. During the synthesis, the precursors for each sample were deposited. Subsequently, the film was annealed in N$_2$ environment for 1 hour to form superlattices. In addition, Samples 2, 3 and 4 were also annealed in Se vapor environment for 3 hours at 400°C, resulting in an improvement of the electrical properties (Lin et al. 2008). To investigate the effect of the annealing in Se environment on the in-plane thermoelectric properties, measurements were carried out on Sample 1 that is of the exact composition as Sample 4, but did not undergo annealing in Se environment. Because of the great enhancement of the electrical conductivity and large Seebeck coefficient after the annealing of the samples in Se, Samples 2,3 and 4 were measured using the four-probe thermoelectric measurement method where the sample is used as a thermocouple element to obtain the contact temperature drops and contact thermal resistance. On the other hand, for Sample 1 that was not annealed in Se the Seebeck coefficient and electrical conductivity were low as shown in Fig. 31, so that the sample cannot be used as a thermocouple element to obtain the contact thermal resistance. Hence, the results for κ and S of this sample are those of the two probe technique.

Table 4.2. Compositions and dimensions of the $[(PbSe)_{0.99}]_x(WSe_2)_x$ film samples.

Sample #	1	2	3	4
Composition	$[(PbSe)_{0.99}]_2(WSe_2)_2$ Annealed in N_2	$[(PbSe)_{0.99}]_3(WSe_2)_3$ Annealed in N_2 and Se	$[(PbSe)_{0.99}]_4(WSe_2)_4$ Annealed in N_2 and Se	$[(PbSe)_{0.99}]_2(WSe_2)_2$ Annealed in N_2 and Se
Unit Cell Size (Å) ± 0.02	25.4	38.1	50.8	25.4
Thickness (nm)	185	115	152	280
Width (nm)	2069	2590	4533	2493
Length (nm)	6184	10853	10083	18246

Figure 30 illustrates the in-plane thermal conductivity κ as a function of temperature for the $[(PbSe)_{0.99}]_x(WSe_2)_x$ samples. Their values are all ~0.4-0.5 W/m K, which is about 5 times higher than the cross-plane thermal conductivity (Chiritescu et al. 2008) and comparable to the minimum thermal conductivity calculated using the speed of sound (Lippmann et al. 1971). This is expected given the nature of this disorder/order structure for films grown by the MERT as explained in the previous section. Additionally the κ appears to be independent of the unit cell size. This is an indication that the in-plane κ is dominated by the surface boundary scattering at the interface between adjacent layers within the unit cell, instead of the interface between two adjacent unit cells. Furthermore, there is only a small difference in the in-plane thermal conductivity between the Sample 1 and 4 that are of the same composition but annealed differently. The slightly lower κ of Sample 1 can be attributed to the fact that the thermal contact resistance could not be subtracted for this sample. Hence, the results suggest that the annealing in Se did not alter

the crystal structure that affects phonon transport.
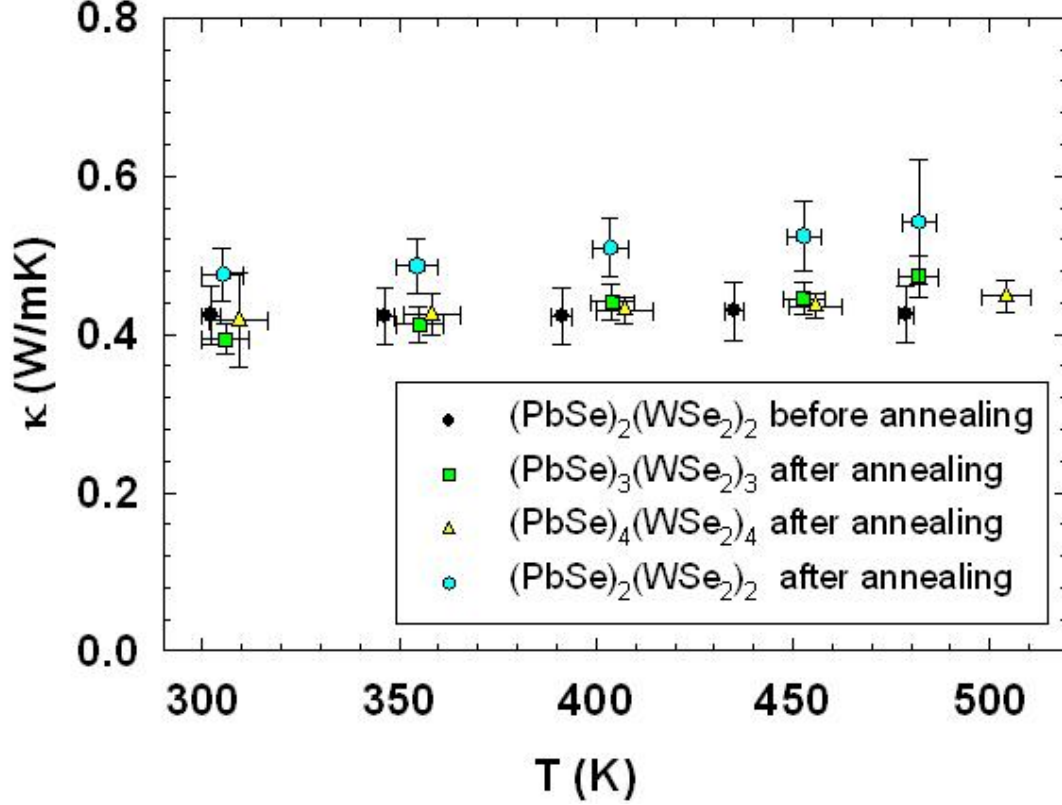
Fig. 30: Measured κ of the $[(PbSe)_{0.99}]_x(WSe_2)_x$ thin films

From Fig. 31(a), σ appears to be weakly dependent on the unit cell size and increases with T suggesting that increasing carrier concentration with T similar to a non-degenerate semiconducting film. All the samples annealed are p-type with a positive Seebeck coefficient that slightly decreases with increasing unit cell size (Fig. 31(b)). For p-type semiconductors

$$S_h = \frac{1}{eT}\left\{E_F - E_V + \left(r + \frac{5}{2}\right)k_B T\right\} \text{(Chen 2005)} \tag{4.1}$$

59

where e is the electron charge, E_F is the Fermi level, E_V is the valence band edge r is the hole scattering rate constant and k_B is the Boltzmann constant. For S to decrease with unit cell size either E_F or r decreases. Since there was no change in the hole scattering mechanisms with unit cell size, then E_F- E_v might have decreased with unit cell size.

Annealing in Se was found to increase the S by one order of magnitude and the σ by two orders of magnitude. These results show that the annealing in Se environment lead to diffusion of Se within the matrix that act as a dopant increasing thus the carrier concentration which in turn enhances σ. However, the observed increased in S upon Se annealing is not well understood. Nevertheless, the annealing in Se environment greatly enhances the power factor without affecting κ which in turn enhances ZT by 3 orders of magnitude (Fig. 32). For the annealed films, however, the in-plane ZT is rather low even though the S is quite high ~250μV/K and the κ is quite low ~0.45 W/m K. The low ZT is attributed to a low σ of ~150 S/m.
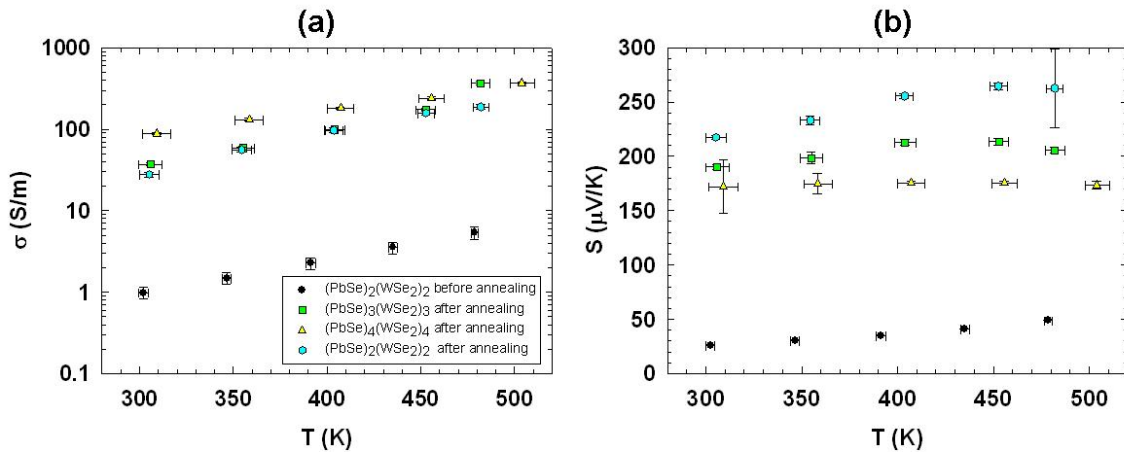
Fig. 31: Measured (a) σ and (b) S of the $[(PbSe)_{0.99}]_x(WSe_2)_x$ thin films.
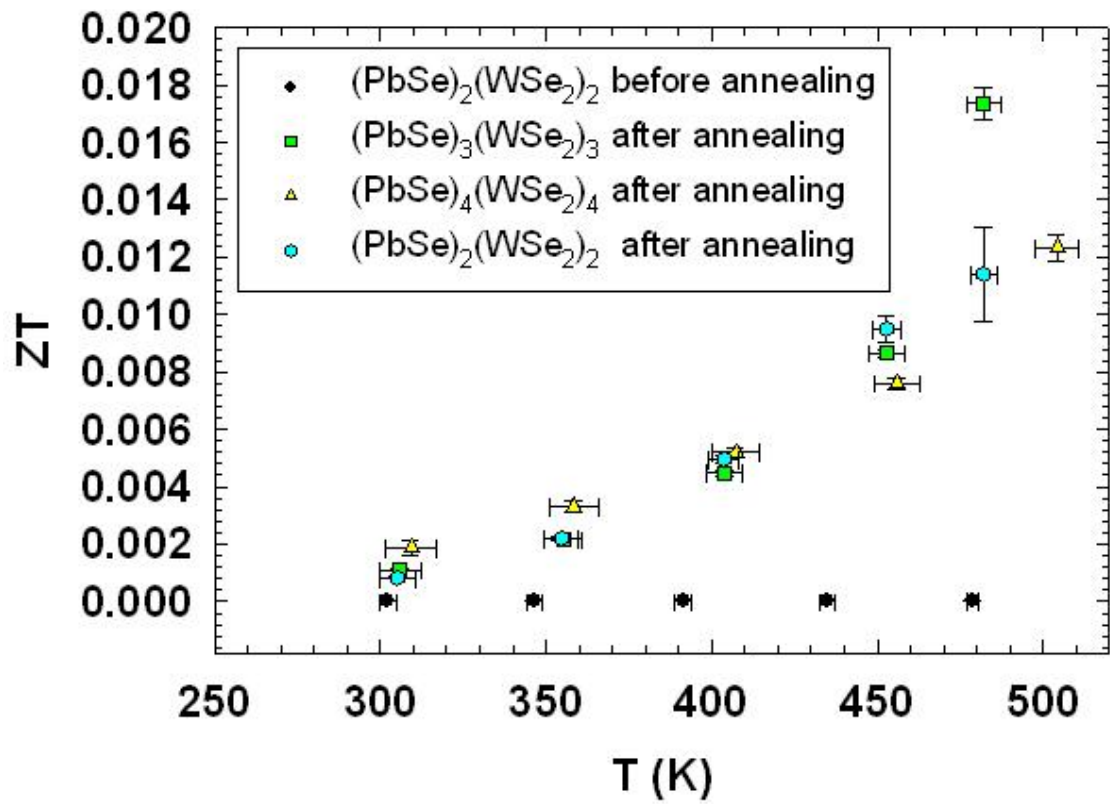
Fig. 32: Measured *ZT* of the $[(PbSe)_{0.99}]_x(WSe_2)_x$ thin films.

4.3   Summary

The characterization method was extended to measure the in-plane thermoelectric properties of disordered layered films including WSe_2, $W_x(WSe_2)_y$ and $(PbSe_{0.99})_x(WSe_2)_x$. These films were grown using the Modulated Elemental Reactant Technique and they exhibited highly anisotropic thermal conductivity. The in-plane thermal conductivity of WSe2 and $W_x(WSe_2)_y$ films was 30 time higher than the cross-plane value reported elsewhere (Chiritescu et al. 2007) whereas the $(PbSe_{0.99})_x(WSe_2)_x$ was about 5 times higher than the cross-plane value (Chiritescu et al. 2008). The reason for this unique anisotropy was the ordered in-plane and disordered cross-plane nature of

the structure that scattered phonons predominantly into the in-plane direction. The WSe_2 films themselves were semi-insulating in nature, but the addition of the W block in the $W_x(WSe_2)_y$ films increased the electrical conductivity 4 orders of magnitude and lattice thermal conductivity by 30%. The $(PbSe_{0.99})_x(WSe_2)_x$ on the other hand were semiconducting with high in-plane Seebeck coefficients. The in-plane thermal conductivity was 5 times higher than the cross-plane values, but independent of unit cell size or x values which shows that the phonon scattering mean free path was dominated by phonon scattering by adjacent layers inside each unit cell. Additionally, annealing the films in Se vapor at 400°C greatly enhanced the power factor of the films without affecting the thermal conductivity. The reason is that the Se diffuses in the film and acts as a dopant.

Chapter 5: Characterizations of the In-Plane Thermoelectric Properties of InAlGaAs films with and without Embedded ErAs Nanoparticles

As discussed in Chapter 1, Shakouri et al. have investigated the use of embedded metallic nanoparticles in a semiconducting III-V matrix to enhance the power factor via an electron filtering effect at the metal-semiconductor Schottky barrier and to scatter phonons to suppress the lattice thermal conductivity (Kim et al. 2006). However, their reported ZT value is based on in-plane power factor and cross-plane thermal conductivity. In this Chapter, both the power factor and thermal conductivity of the nanoparticle composite film have been measured in the in-plane direction using the method described in Chapter 2. The measurement results are compared with those by Zeng et al. (Zeng et al. 2007)

5.1   Sample Preparation

The ErAs:(InGaAs)1-x(InAlAs)x samples were grown by Zide et al. (Zide et al. 2005) using a Varian Gen III MBE system on lattice-matched (100) InP substrates. The growth rate was about 2 lm per hour and the growth temperature was maintained at 490 °C. The ErAs:$(InGaAs)_{1-x}(InAlAs)_x$ is n-type consisting of 80% InGaAs and 20% InAlAs. The ErAs concentration is 0.3% by volume. The ErAs impurity doping levels were designed to be $9x10^{18}$ cm^{-3}. A reference sample was also grown with the exact same composition without the ErAs nanoparticles for comparison. Both types of samples were grown to a thickness of 500 nm.

Individual thin films were patterned as illustrated in Fig. 33. Electron Beam Lithography (EBL) was used to pattern arrays of Poly-methyl-methacrylate (PMMA) resist lines of different widths ranging from 0.5 to 2 μm and lengths ranging from 20 to 35 μm. This resist pattern was used as an etching mask during the etching of the InGaAlAs film in a citric acid/hydrogen peroxide ($C_6H_8O_7/H_2O_2$) solution. For etchant preparation, 24 grams of citric acid were diluted in 10ml of de-ionized water (DIH_2O) and let to rest overnight since it is an endothermic reaction (Lijadi et al. 2005). During the next day, the citric acid/de-ionized (DI) H_2O solution was mixed with H_2O_2 at a ratio of 2:1. This solution produced an etching rate of ~100 nm/min for an InGaAlAs film. The sample with the PMMA pattern was immersed in the solution for 5 minutes to transfer the pattern completely to the 500 nm thick InGaAlAs:ErAs film. After the pattern was transferred to the film, the residual resist was stripped in hot acetone at 60°C for 15 minutes. The underlying InP substrate was etched away in a diluted HCl solution (3:1 HCl:DIH_2O) for 20 minutes. Since the HCl:DI H_2O solution etches InP anisotropically, the EBL patterning of the PMMA was carried out at an angle relative to the cleaved edge of the InP substrate so as to avoid creating etching stop surfaces as illustrated in Fig. 34.
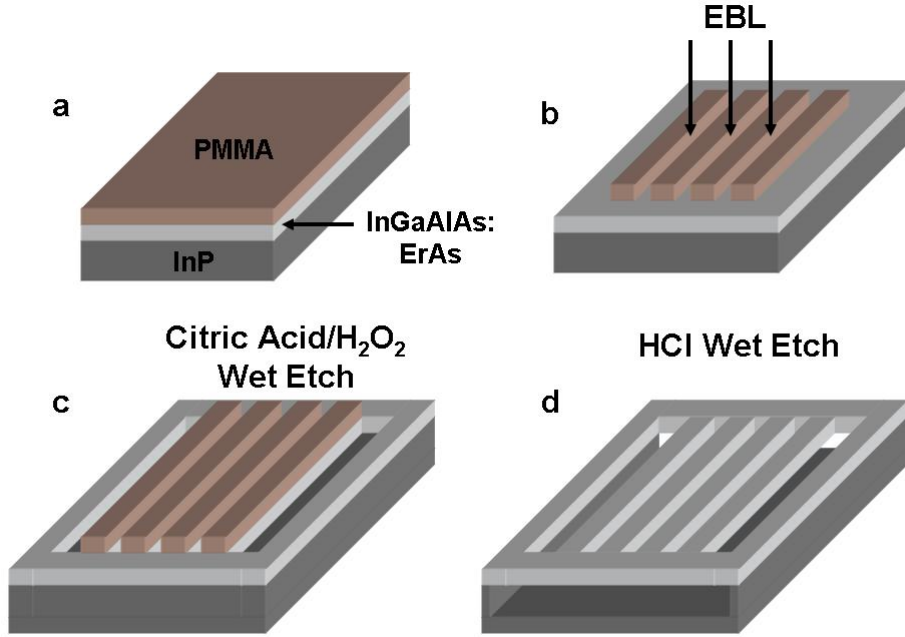
Fig. 33: Fabrication process to pattern individual III-V individual thin film segments.
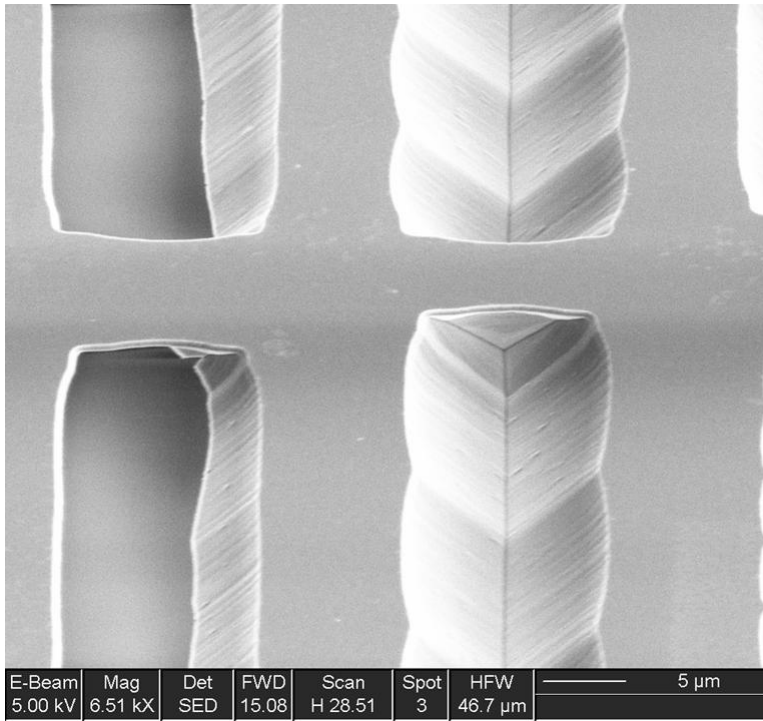
Fig. 34: SEM of the anisotropic etching of the InP substrate in HCl:DIH$_2$O solution.

The thin films were transferred to the suspended micro-device using a Zyvex S100 Nanomanipulator System as explained in Chapter 4. Since the individual InGaAlAs:ErAs thin film segments were suspended from the substrate, the nanomanipulator tip was able to easily break off an individual thin film segment and transfer it directly to the suspended micro-device as illustrated in Fig. 35. To enhance the electrical and thermal contact to the micro-device we used Electron Beam Induced Metal Deposition (EBIMD) to deposit 250 nm wide, 750 nm thick, 2 μm long Pt lines on top of the thin film and each of the four underlying Pt electrodes pre-patterned on the suspended device, as illustrated in Fig. 36.
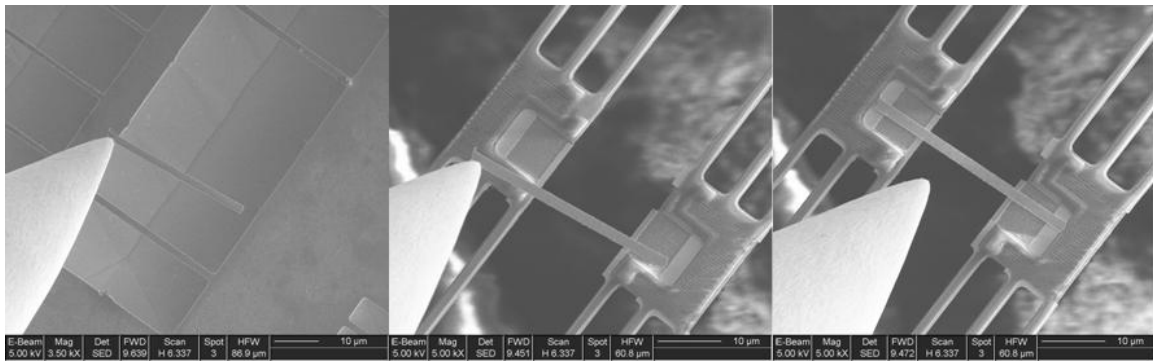
Fig. 35: Transfer of patterned thin film to the micro-device using the nanomanipulator system.
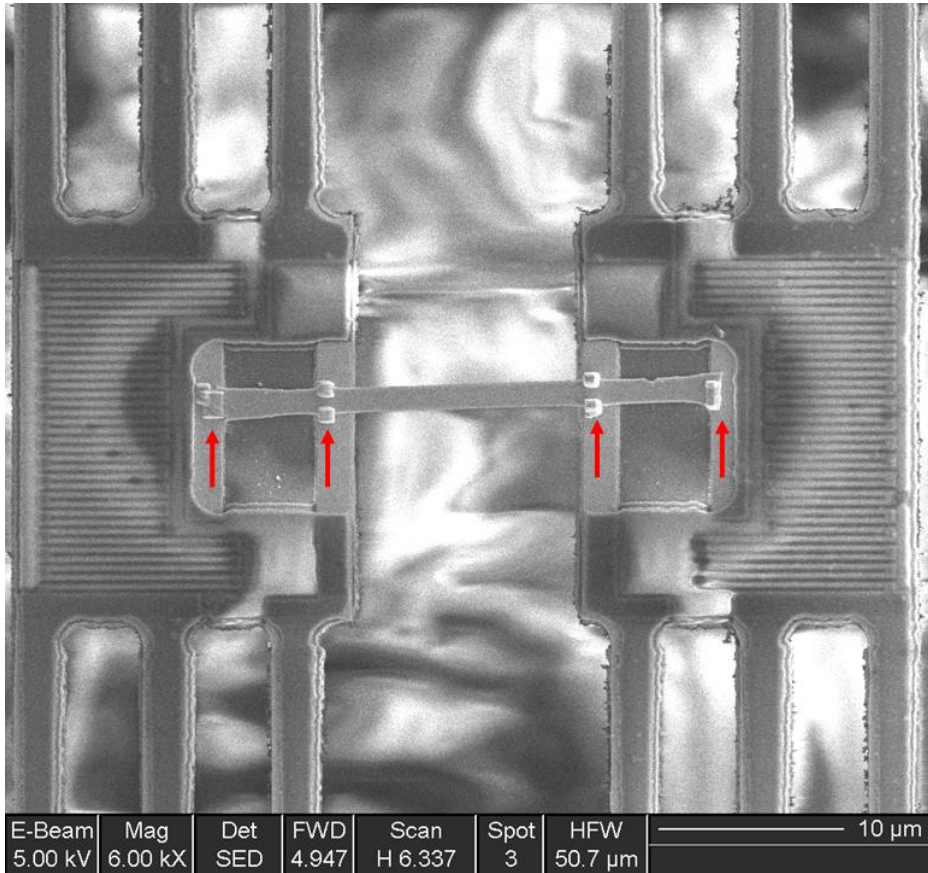
Fig. 36: SEM of an assembled patterned InGaAlAs:ErAs thin film. The arrows indicate the four Pt depositions on top of the contacts between the thin film and the electrodes.

Three samples were prepared for the in-plane measurement. Two samples were 500 nm thick InGaAlAs films embedded with 0.3% ErAs nanoparticles. The other sample was a 500 nm thick InGaAlAs sample without any particles, labeled as reference sample. After the thermoelectric characterization was performed, the thickness of each individual thin film segment was measured by Atomic Force Microscopy (AFM). AFM was performed on each thin film segment while still on the suspended microdevice. The final thickness for the ErAs nanoparticles sample was 300±10 nm whereas for the reference

sample this was 400 nm. The reduced film thickness is caused by the wet etching process. The citric acid/hydrogen peroxide solution etches InGaAlAs isotropically therefore the film is etched under the PMMA mask. This causes a thickness reduction of the individual thin film segments under the PMMA pattern. The measured thickness results also indicated that the etching solution etches the nanoparticles sample faster than the reference sample, probably because the nanoparticles create a small amount of strain within the matrix of the film that causes it to react faster with the etching solution.

5.2   Thermoelectric Characterization

Thermoelectric measurements of the three samples were performed.   The measurement results are plotted in Fig. 37 together with the published results by Zeng et al. for a 2 μm thick InGaAlAs film with 0.3% ErAs nanoparticles (Zeng et al. 2007). Zeng et al's results were obtained from different batches of samples on top of an InP semi-insulating substrate. The thermal conductivity was the cross-plain values obtained with the 3ω technique; whereas the S and σ were the in-plane values.

As shown in Fig. 37(a), the S of the samples with embedded nanoparticles is 50% lower than that of the reference sample without the nanoparticles. On the other hand (Fig. 37(b)), the σ of the sample with nanoparticles is 2-3 orders of magnitude higher than the reference sample, resulting in 1 order of magnitude enhancement in the power factor.

Furthermore, Figure 37 shows that both the electrical conductivity and Seebeck coefficient of the increase with temperature, for both our results and Zeng et al.'s results (Zeng et al. 2007). In typical degenerate semiconductors, the electrical conductivity

decreases with temperature because of electron-phonon scattering; whereas the Seebeck coefficient increases with temperature because of the increase of the diffusion thermo-power with temperature. In the InAlGaAs films with embedded ErAs nanoparticles, the increase of both electrical conductivity and Seebeck coefficient with temperature can be attributed to the electron filtering effect by the Schottky barrier at the interface between the nanoparticles and the host. As temperature increases, thermionic emission of hot electrons over the potential barrier increases the electrical conductivity without reducing the Seebeck coefficient. The electron filtering effect helps to increase the power factor. The increasing S and σ with T caused by the electron filtering effect is not observed in the reference samples.

Although the two measurement results show similar temperature dependences, our measured in-plane S and σ of the ~300 nm thick films with embedded nanoparticles are about 30% lower than those measured by Zeng et al. on 2 μm thick films on an INP substrate. The difference can be caused by two factors. First of all, electron-surface scattering in our thinner film can suppress the mobility and σ, and affect S. Secondly, the semiconducting InP substrate of Zeng et al.'s film might also contribute to their measured electrical conductance and S of the film sample.
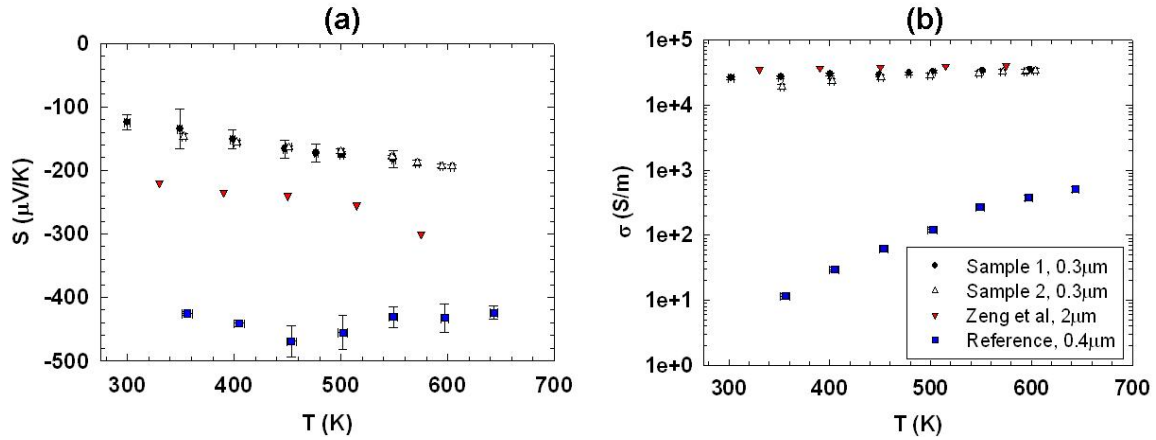
Fig. 37: Measured electrical conductivity (a), Seebeck coefficient (b) of two 300 nm thick InAlGaAs film samples with embedded ErAs nanoparticles as a function of temperature. Also shown are in-plane electrical conductivity and Seebeck coefficient of 2μm thick InGaAlAs:ErAs films. The two figures share the same legend in shown in (b).

Figure 38(a) shows the thermal conductivity as a function of temperature. At a temperature of about 575 K, the in-plane thermal conductivity of the 300 nm films with embedded ErAs nanoparticles is close to the cross-plane values reported by Zeng et al. for a 2 μm thick film. However, it is interesting to note that the in-plane thermal conductivity of the suspended film peaks around 450-600K range, while the peak in the cross-plane κ of the thicker film is at below room temperature. The shifting of the peak temperature can be attributed to increased surface scattering of phonons and consequently reduced phonon mean free path in the thinner film. Because of Umklapp phonon scattering, the thermal conductivity of bulk semiconductors decreases with increasing temperature at temperature above a fraction of the Debye temperature. As the mean free path is reduced by additional surface scattering, the effect of Umklapp phonon-phonon

scattering becomes apparent only at a much higher temperature where the Umklapp phonon scattering mean free path becomes shorter than the boundary scattering mean free path. Zeng et al. has reported that the embedded nano-particles can greatly suppress the cross-plane thermal conductivity (Zeng et al. 2007). However, the cross-plane thermal conductivity of the films with embedded nanoparticles is only slightly lower than that of the reference sample without the embedded nanoparticles. At the presence, we are not able to explain this discrepancy.

The *ZT* results for all the samples are plotted in Fig. 38(b). Overall the ErAs nanoparticles samples show an enhancement of *ZT* 3 orders of magnitude over the reference sample. The enhancement is caused by the increase of σ due to the incorporation of the nanoparticles in the matrix that act as dopants, as well as the thermionic emission effect that leads to both increasing S and σ with T. The peak in-plane *ZT* found in the 300 nm film was 0.3 at a temperature of 600 K. This value is ~2.5 times lower than the result reported by Zeng et al. calculated using the in-plane power factor and cross-plane thermal conductivity of thicker films on an INP substrate. The discrepancies can be caused by four factors. Firstly, increased electron-surface scattering in our thinner films could have reduced the power factor. Secondly, the wet etching or Pt deposition processed used for preparing the suspended film sample could have altered the property of the sample. Thirdly, the thermal conductivity of the film can be anisotropic. Lastly, Zeng et al.'s measured in-plane power factor of the film could consist of a contribution from the semi-insulating substrate.
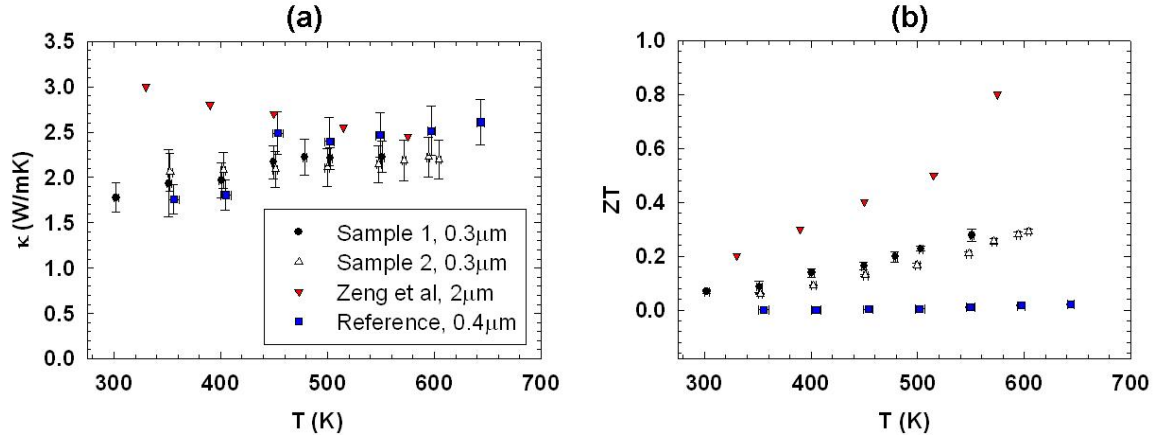
Fig. 38: Measured thermal conductivity (a), *ZT* (b) of two 300 nm thick InAlGaAs film samples with embedded ErAs nanoparticles as a function of temperature. Also shown are cross-plane thermal conductivity and *ZT* of 2 μm thick InGaAlAs:ErAs films. The two figures share the same legend in shown in (a).

5.3   Summary

Semiconducting films of InGaAlAs with and without embedded metallic ErAs nanoparticles were characterized using the suspended micro-device. These nanoparticles were used to filter out low energy electrons with the introduction of Schottky barriers so as to increase the power factor ($S^2\sigma$) and scatter long to mid range phonons and thus suppress κ. The in-plane measurements showed that both the S and σ increase with increasing temperature because of the electron filtering effect. The films with the nanoparticles exhibited an increase in σ by three orders of magnitude and a decrease in S by only fifty percent compared to the films without, suggesting that the nanoparticles acted as dopants within the film. On the other hand, the measured in-plane κ showed little

difference between the films with and without nanoparticles, different from findings

based on published cross-plane thermal conductivity results (Zeng et al. 2007).

Chapter 6: Conclusions

This dissertation describes the development of a method for combined structure and thermoelectric characterization of individual nanowires and thin films, which are investigated for enhancing the thermoelectric figure of merit (ZT). An improved design of a suspended microdevice was batch fabricated for four-probe measurement of electrical conductivity, thermal conductivity, and Seebeck coefficient of individual nanowires assembled on the device. The method was extended to thin films to measure the in-plane thermoelectric properties. With the use of the sample itself as a thermocouple element to measure the contact temperature drop, a new procedure was developed to eliminate the errors caused by contact thermal resistance in the measured thermal conductivity and Seebeck coefficient. Furthermore, an etch-though hole was formed in the substrate below the suspended device to allow for TEM and EDS characterization of the crystal structure and chemical composition of the sample, so as to establish the structure-transport property correlation of the sample.

Measurements were performed on 4 different individual $Bi_{1-x}Te_x$ nanowires with a nominal diameter of about 55 nm. A method based on annealing the sample in forming gas was developed to make electric contact between the nanowire and the underlying electrodes. The measured thermoelectric properties were found to depend on the nanowire crystalline quality and impurity doping concentration. Higher electrical conductivity and *ZT* were found in nanowires of good crystalline quality. All the nanowires were found to be n type with high carrier concentration of $2\text{-}4\text{x}10^{19}$ cm^{-3}.

Additionally, of the thermal conductivity was suppressed on three out of the four samples. The reason for the lower thermal conductivity was attributed to poor crystal quality and/or enhanced surface phonon scattering which suppresses both the electronic as well as the lattice contribution to the thermal conductivity. Because of defects and high carrier concentration in the nanowires, the highest ZT measured was 0.3 and lower than that of bulk single crystals at the optimum carrier concentration. Additionally a suppression of the κ was demonstrated in one nanowire compared to other nanowires, without significant suppression of the electrical properties, resulting in the highest ZT in this nanowire. The mechanism for this preferential suppression is not well understood.

The characterization method was used to measure the in-plane thermoelectric properties of disordered, layered thin films grown by the Modulated Elemental Reactant Technique (MERT), including WSe_2, $W_x(WSe_2)_y$, and $(PbSe_{0.99})_x(WSe_2)_x$ films. These films exhibited highly anisotropic thermal conductivity. For example, the in-plane thermal conductivity of the WSe_2 films was about 30 times higher than cross-plane value measured elsewhere using the time domain thermal reflectance (TDTR) method. The reason for this increased anisotropy compared to the corresponding bulk single crystals was the in-plane ordered, cross-plane disordered nature of the structure, which was validated through HRTEM on the sample for which the thermal measurement was made. The extremely low cross-plane thermal conductivity found in the film may be attributed to the in-plane ordered, cross-plane disordered structure, which lead to phonons scattered predominantly into the in-plane direction. Adding W blocks in the film to form disordered, layered $W_x(WSe_2)_y$ films increased the electrical conductivity by 4 orders of

magnitude, reduced the lattice thermal conductivity by about 30 percent, and retained a similar anisotropic thermal conductivity.

While the WSe_2 and $W_x(WSe_2)_y$ films were semi-insulating and metallic, respectively, the $(PbSe_{0.99})_x(WSe_2)_x$ superlattice thin films were semiconductors with high Seebeck coefficients along the in-plane direction. Four different $(PbSe_{0.99})_x(WSe_2)_x$ samples of different unit cell sizes or x values were characterized. The in-plane thermal conductivity was 5 times higher than the cross-plane values, and independent of the unit cell size. This indicates that the phonon scattering mean free path was dominated by phonon scattering by adjacent layers inside each unit cell instead of at the interfaces between two adjacent unit cells. Additionally, annealing the films in Se vapor at 400°C greatly enhanced the electrical properties of the films without affecting the thermal conductivity. The reason is that the Se diffuses in the film and acts as a dopant.

The characterization method has also been employed to measure the in-plane thermoelectric properties of semiconducting InAlGaAs films with and without embedded metallic ErAs particles. The ErAs were used to filter low energy electrons with the introduction of Schottky barriers, so as to increase the power factor. They were also designed to scatter mid to long wavelength phonons in order to suppress the lattice thermal conductivity. The electron filtering effect was validated by the in-plane measurement results, which showed increasing electrical conductivity and Seebeck coefficient with increasing temperature. The samples with embedded ErAs nanoparticle exhibited electrical conductivities 3 orders of magnitude higher than the samples without the nanoparticles, suggesting that the nanoparticles acted as dopants within the film as

well. The in-plane electrical conductivity and Seebeck coefficient measured on the 300 nm thick films with embedded ErAs nanoparticles showed a similar temperature dependence, but were 30 percent lower than those reported for 2 μm thick films on a semi-insulating InP substrate. The different magnitudes could be caused by several factors. Firstly, increased electron-surface scattering in the thinner films could have reduced the power factor. Secondly, the wet etching or Pt deposition processed used for preparing the suspended film sample could have altered the property of the sample. Lastly, the measured in-plane power factor of the film on the substrate could consist of a contribution from the semi-insulating substrate. Furthermore, the measured in-plane thermal conductivity of the suspended films showed little difference between the samples with and without the nanoparticles, different from the finding based on the published cross-plane thermal conductivity results. The cause of the discrepancy is not understood at the present time.

```matlab
function y=GamaAlpha
%all the U values are the absolute not the relative values
%copy data from GamaAlphaDataTemplate
A = [
63.23201966 1.457052634
-240.4686409    -3.13912537
-232.4597948    -3.205120985
16317.53333 232.9075131
8543.653333 137.2584839
1059.56 19.01926
780.3066667 143.1416117
8445.63 89.43575109
9060.616667 48.52770663
9034.083333 191.8848673
];

Gtotal = A(1,1);
UGtotal = A(1,2);
S14 = A(2,1);
Us14 = A(2,2);
S23 = A(3,1);
Us23 = A(3,2);
Ls = A(4,1)*1e-3;
ULs = A(4,2)*1e-3;
L1 = A(5,1)*1e-3;
UL1 = A(5,2)*1e-3;
L2 = A(6,1)*1e-3;
UL2 = A(6,2)*1e-3;
L3 = A(7,1)*1e-3;
UL3 = A(7,2)*1e-3;
L4 = A(8,1)*1e-3;
UL4 = A(8,2)*1e-3;
Lc1 = A(9,1)*1e-3;
ULc1 = A(9,2)*1e-3;
Lc2 = A(10,1)*1e-3;
ULc2 = A(10,2)*1e-3;

gama = S14/S23;
Ugama = gama* sqrt ((Us14/S14)^2 + (Us23/S23)^2);

[m0, alpha0, gama23_0] = alp(gama, Ls, L1, L2, L3, L4, Lc1, Lc2);

[m1, alpha1, gama23_1] = alp(gama + Ugama, Ls, L1, L2, L3, L4, Lc1,
Lc2);

[m2, alpha2, gama23_2] = alp(gama, Ls + ULs, L1, L2, L3, L4, Lc1, Lc2);

[m3, alpha3, gama23_3] = alp(gama, Ls, L1 + UL1, L2, L3, L4, Lc1, Lc2);

[m4, alpha4, gama23_4] = alp(gama, Ls, L1, L2 + UL2, L3, L4, Lc1, Lc2);
```

```
[m5, alpha5, gama23_5] = alp(gama, Ls, L1, L2, L3 + UL3, L4, Lc1, Lc2);

[m6, alpha6, gama23_6] = alp(gama, Ls, L1, L2, L3, L4 + UL4, Lc1, Lc2);

[m7, alpha7, gama23_7] = alp(gama, Ls, L1, L2, L3, L4, Lc1 + ULc1,
Lc2);

[m8, alpha8, gama23_8] = alp(gama, Ls, L1, L2, L3, L4, Lc1, Lc2 +
ULc2);


Um1 = m1 - m0;
Um2 = m2 - m0;
Um3 = m3 - m0;
Um4 = m4 - m0;
Um5 = m5 - m0;
Um6 = m6 - m0;
Um7 = m7 - m0;
Um8 = m8 - m0;


U1 = alpha1 - alpha0;
U2 = alpha2 - alpha0;
U3 = alpha3 - alpha0;
U4 = alpha4 - alpha0;
U5 = alpha5 - alpha0;
U6 = alpha6 - alpha0;
U7 = alpha7 - alpha0;
U8 = alpha8 - alpha0;


Ug1 = gama23_1 - gama23_0;
Ug2 = gama23_2 - gama23_0;
Ug3 = gama23_3 - gama23_0;
Ug4 = gama23_4 - gama23_0;
Ug5 = gama23_5 - gama23_0;
Ug6 = gama23_6 - gama23_0;
Ug7 = gama23_7 - gama23_0;
Ug8 = gama23_8 - gama23_0;


gama
Ugama
UgamaRelative = Ugama/gama

alpha = alpha0
Ualpha = sqrt(U1^2 + U2^2 + U3^2 + U4^2 + U5^2 + U6^2 + U7^2 + U8^2)
UalphaRelative = Ualpha/alpha0

gama23 = gama23_0
Ugama23 = sqrt(Ug1^2 + Ug2^2 + Ug3^2 + Ug4^2 + Ug5^2 + Ug6^2 + Ug7^2 +
Ug8^2)
Ugama23Relative = Ugama23/gama23
```

```
m = m0
Um = sqrt(Um1^2 + Um2^2 + Um3^2 + Um4^2 + Um5^2 + Um6^2 + Um7^2 +
Um8^2)
UmRelative = Um/m0


S = alpha*S23/gama23
Us = S*sqrt((Us23/S23)^2 + (Ualpha/alpha)^2 + (Ugama23/gama23)^2)
UsRelative = Us/S


Gs = Gtotal*alpha
UGs = Gs*sqrt((UGtotal/Gtotal)^2+(Ualpha/alpha)^2)
UGsRelative = UGs/Gs


Rc = 1/Gtotal - 1/Gs;
URc = sqrt((UGtotal/(Gtotal*Gtotal))^2 + (UGs/(Gs*Gs))^2);
URcRelative = URc/Rc;


Gc = 1/Rc
UGc = Gc* URcRelative
UGcRelative = URcRelative
```

APPENDIX B

```matlab
function [m, alpha, gama23] = alp(gama, Ls, L1, L2, L3, L4, Lc1, Lc2)
%all the lengths should be given in nm in AlphaGamaData, and are
converted
%to um before calling this alp funciton

m0 =0.01;
dm =1e-3;
if gama<1.4
    m0 =0.1;
    dm =1e-2;
end
m=fzero(@(m)(gama-(1+(1-cosh(m*(Lc1-
L1))/cosh(m*Lc1))/(Ls*m*tanh(m*Lc1))+(1-cosh(m*(Lc2-
L4))/cosh(m*Lc2))/(Ls*m*tanh(m*Lc2)))/(1+(1-cosh(m*(Lc1-
L2))/cosh(m*Lc1))/(Ls*m*tanh(m*Lc1))+(1-cosh(m*(Lc2-
L3))/cosh(m*Lc2))/(Ls*m*tanh(m*Lc2)))), m0);
if m<0
    m = -1*m;
end
alpha = 1+1/(Ls*m*tanh(m*Lc1))+1/(Ls*m*tanh(m*Lc2));
gama23 = gama_ij(m, Ls, L2, L3, Lc1, Lc2);
```

APPENDIX C

Uncertainty Analysis

To improve the measurement uncertainty, we ramped I from zero to a negative maximum $(-I_{max})$, from $-I_{max}$ back to zero, from zero to a positive maximum (I_{max}), and from I_{max} back to zero. One ramping cycle took about 11 minutes. During each ramping cycle, a total number of $N = 203$ sets of measurements were taken. G_b was obtained as the slope of a least-square linear curve fit of $Q \equiv (Q_h + Q_L)$ as a function of $(\Delta T_h + \Delta T_s)$. The ratio G_{total}/G_b was then obtained as the slope of a linear curve fit of the measured ΔT_s as a function of the measured $(\Delta T_h - \Delta T_s)$. G_m is then obtained as $G_{total} = G_b(G_{total}/G_b) = G_b b_1$, where $b_1 \equiv G_{total}/G_b$.

The uncertainty in each G_{total} measurement, i.e. $U_{G_{total}}$, was calculated from the uncertainties in G_b and $b_1 \equiv G_{total}/G_b$, i.e. $U_{G_{total}}$ and U_{b_1} (or U_{G_{total}/G_b}) based on uncertainty propagation:

$$U_{G_{toal}} = \sqrt{\left(\frac{\partial G_{total}}{\partial G_b} U_{G_b}\right)^2 + \left(\frac{\partial G_{total}}{\partial b_1} U_{b_1}\right)^2} \qquad (15a)$$

which can be reduced to the following for the case that $G_{total} = G_b b_1$

$$\frac{U_{G_{toal}}}{G_{toal}} = \sqrt{\left(\frac{U_{G_b}}{G_b}\right)^2 + \left(\frac{U_{G_{total}/G_b}}{G_{total}/G_b}\right)^2} \qquad (15b)$$

$U_{G_{total}}$ and U_{G_{total}/G_b} were calculated as the uncertainties in the slope of the corresponding least-square linear fitting according to the error propagation method of

82

Coleman and Steele [1]. For $N(X_i, Y_i)$ data pairs, the slope (m) of a least-square linear curve fit is determined as

$$m = \frac{N\sum_{i=1}^{N} X_i Y_i - \sum_{i=1}^{N} X_i \sum_{i=1}^{N} Y_i}{N\sum_{i=1}^{N} (X_i^2) - \left(\sum_{i=1}^{N} X_i\right)^2} \tag{16}$$

The uncertainty in m is calculated as

$$\begin{aligned}
U_m^2 &= \sum_{i=1}^{N}\left(\frac{\partial m}{\partial Y_i}\right)^2 P_{Y_i}^2 + \sum_{i=1}^{N}\left(\frac{\partial m}{\partial X_i}\right)^2 P_{X_i}^2 + \sum_{i=1}^{N}\left(\frac{\partial m}{\partial Y_i}\right)^2 B_{Y_i}^2 + 2\sum_{i=1}^{N-1}\sum_{k=i+1}^{N}\left(\frac{\partial m}{\partial Y_i}\right)\left(\frac{\partial m}{\partial Y_k}\right) B_{Y_i Y_k} \\
&+ \sum_{i=1}^{N}\left(\frac{\partial m}{\partial X_i}\right)^2 B_{X_i}^2 + 2\sum_{i=1}^{N-1}\sum_{k=i+1}^{N}\left(\frac{\partial m}{\partial X_i}\right)\left(\frac{\partial m}{\partial X_k}\right) B_{X_i X_k} + 2\sum_{i=1}^{N}\sum_{k=1}^{N}\left(\frac{\partial m}{\partial X_i}\right)\left(\frac{\partial m}{\partial Y_k}\right) B_{X_i Y_K}
\end{aligned} \tag{17}$$

where P_{Y_i} (or P_{X_i}) is the random or precision uncertainty for the Y_i (or X_i) variable, B_{Y_i} (or B_{X_i}) is the systematic or bias uncertainty for the Y_i (or X_i) variable, $B_{Y_i Y_k}$ (or $B_{X_i X_k}$) is the covariance estimator for correlated systematic uncertainties in the Y_i and Y_k variables (or the X_i and X_k variables), and $B_{X_i Y_k}$ is the covariance estimator for correlated systematic uncertainties between X_i and Y_k.

During each ramping cycle of the measurement, four (X_i, Y_i) data sets were measured at the same I magnitude. The random uncertainties are calculated as $P_{Y_i} = t_{v,95} S_{Y_i}$ and $P_{X_i} = t_{v,95} S_{X_i}$, where $t_{v,95} = 3.182$ is the t distribution for a $v = 3$ degree of freedom corresponding to a sample size of four at a probability or confidence level of 95%, and S_{Y_i} (or S_{X_i}) is the sample standard deviation of the four Y_i (or X_i) measurement results at the same I magnitude.

As discussed by Brown et al. [2], systematic errors that are a fixed value or "percent of full scale" have no influence on the uncertainty of the slope and thus do not need to be included in Eq. (17). On the other hand, a systematic error of a second type that is a function of the magnitude of the variables, such as those of a "percent of reading" nature, can cause a non-zero systematic uncertainty in the slope of the linear curve fit. This second type of systematic errors in the measurement results of ΔT_h, ΔT_s, Q_L, and Q_h were identified and calculated as following.

First, the Pt RT was calibrated with one of the two factory-calibrated silicon diodes in the cryostat serving as the reference temperature (T_f). The specified uncertainty of T_f is $U_{T_f} = 0.01\%T_f$ including both random and systematic errors. Due to a small temperature gradient in the cryostat, there was a less than 0.2% difference between the temperature readings of the two diodes that were located 4.5 cm apart from each other. The RT on the micro-device was located between the two diodes and the diode right next to the RT was used as the reference in the temperature calibration. The difference between T_f and the actual temperature of the RT should be less than 0.2% because the distance between the RT and the reference diode was much shorter than that between the two diodes. Thus, the systematic error in the calibration of the RT was calculated to be $B_T \leq 0.2\%T$. Because $B_{T_h(I)}$ and $B_{T_h(I=0)}$ arise from the same calibration error and are thus perfectly correlated, the propagation of $B_{T_h(I)} \leq 0.2\%T_h(I)$ and $B_{T_h(I=0)} \leq 0.2\%T_h(I=0)$ results in $B_{\Delta T_h(I)} \leq 0.2\%\Delta T_h(I)$ [1]. In another word, because $T_h(I)$ and $T_h(I=0)$ were distorted by the same percent of the reading due to the same calibration error in the

reference temperature, $\Delta T_h(I)$ was distorted by the same percent of the reading. Similarly, $B_{\Delta T_s(I)} \leq 0.2\% \Delta T_s(I)$. Because T_h and T_s are calibrated using the same T_f and thus B_{T_h} and B_{T_s} arise from the same calibration error, B_{T_h} and B_{T_s} are also perfectly correlated and propagate into $B_{(\Delta T_h - \Delta T_s)} \leq 0.2\%(\Delta T_h - \Delta T_s)$ and $B_{(\Delta T_h + \Delta T_s)} \leq 0.2\%(\Delta T_h + \Delta T_s)$.

The Joule heat Q was obtained based on the measured voltage drop across the heating PRT and the two leads (V_d) and current (I), and the measured resistance (R_h) of the heating PRT, according to

$$Q \equiv I^2 R_h + (IV_d - I^2 R_h)/2 = (IV_d + I^2 R_h)/2 \tag{18}$$

The bias uncertainty is calculated to be $B_Q \approx 0.6\% Q$, which is dominated by the 1% gain uncertainty of the AC output and input of the lock-in amplifier that is used for measuring R_h.

For each fitting step, Y_i and Y_k were measured using the same instrument. Hence, B_{Yi} and B_{Yk} arise from the identical error sources and are perfectly correlated, i.e. $B_{Y_i Y_k} = B_{Y_i} B_{Y_k}$. Similarly, $B_{X_i X_k} = B_{X_i} B_{Xk}$. For the fitting step for obtaining G_b, B_{X_i} (or $B_{(\Delta T_h + \Delta T_s)}$) and B_{Y_k} (or B_Q) are not correlated, and thus $B_{X_i Y_k} = 0$. For the fitting step for obtaining G_{total}/G_b, B_{X_i} (or $B_{\Delta T_s}$) and B_{Y_k} (or $B_{(\Delta T_h - \Delta T_s)}$) are perfectly correlated, and thus $B_{X_i Y_k} = B_{X_i} B_{Y_k}$. For the fitting step for obtaining S_{14} or S_{23}, B_{X_i} (or $B_{(\Delta T_h - \Delta T_s)}$) and B_{Y_k} (or B_{V14} or B_{V14}) are not correlated, and thus $B_{X_i Y_k} = 0$.

The dominant uncertainty source is the random fluctuation in the temperature measurement. This fluctuation was observed to be about 40×10^{-3} K. The random

fluctuation was caused by the temperature fluctuation of the evaluated cryostat where the sample was located as well as the random uncertainty of the lock-in amplifier used to measure the differential electrical resistance of the RT.

To reduce the uncertainty, for each measurement we often needed to spend hours to reduce the temperature fluctuation of the cryostat below 40×10^{-3} K and used a sufficiently large ΔT_h value of about 2K or more to obtain $U_{G_{total}}/G_{total}$ <10%. Moreover, three or more measurements are made at each temperature. If we obtained less than three measurement results with $U_{G_{total}}/G_{total}$ <10% at the same temperature, the G_{total} result with the lowest $U_{G_{toal}}/G_{toal}$ is reported. If we obtained there or more measurement results with $U_{G_{total}}/G_{total}$ <10% at one temperature, the averaged value ($\overline{G_{total}}$) of the several measurements is reported because the random uncertainty is reduced with increasing number (n) of measurements. The total uncertainty in $\overline{G_{total}}$ is calculated as

$$U_{\overline{G_{total}}} = (P_{\overline{G_{total}}}{}^2 + B_{\overline{Gtotal}}{}^2)^{1/2} \tag{19}$$

where the random uncertainty in $\overline{G_m}$ is calculated as

$$P_{\overline{G_{total}}} = t_{n-1,95}S_{G_{total}}/\sqrt{n} \tag{20}$$

where S_{G_m} is the sample standard deviation of the n measurements of G_m, and $t_{n-1,95}$ is the t distribution for n-1 degree of freedom and a confidence level of 95%.

In Eq. (20), $B_{\overline{G_{total}}}$ is the systematic of the second type in $\overline{G_{total}}$.

Because $B_{G_{total}}/G_{total}$ is the same for each measurement, $B_{\overline{G_{total}}}/\overline{G_{total}} = B_{G_{total}}/G_{total}$. In the fitting to obtain G_{total}/G_b, $B_{(\Delta T_h - \Delta T_s)}$ and $B_{\Delta T_s}$ are perfectly correlated because they share the same error source, i.e. the calibration error due to the same B_{T_f}. In another word, the obtained X and Y variables were distorted by the same percent of the reading, or $B_{(\Delta T_h - \Delta T_s)}/(\Delta T_h - \Delta T_s) = B_{\Delta T_s}/\Delta T_s$. Consequently, the slope G_{total}/G_b is not affected by this calibration error, or $B_{G_{total}/G_b} = 0$. Therefore, $B_{G_{total}}/G_{total} = \sqrt{(B_{G_b}/G_b)^2 + (B_{G_{total}/G_b}/(G_{total}/G_b))^2} = B_{G_b}/G_b$. For the fitting step for obtaining G_b, $B_{(\Delta T_h + \Delta T_s)}$ and $B_{(\Delta T_h + \Delta T_s)}$ are not correlated. Thus

$$\frac{B_{\overline{G_{total}}}}{\overline{G_{total}}} = \frac{B_{G_{total}}}{G_{total}} = \frac{B_{G_b}}{G_b} = \sqrt{\left(\frac{B_{(\Delta T_h + \Delta T_s)}}{\Delta T_h + \Delta T_s}\right)^2 + \left(\frac{B_Q}{Q}\right)^2} \tag{21}$$

If three or more data sets are obtained, we can use the Excel template with three data sets to obtain $U_{\overline{G_{total}}}$ according to Equation 21 and $U_{\overline{S_{14}}}$ or $U_{\overline{S_{23}}}$ according to a similar procedure.

If we have more than three good data sets, we obtain G_s, R_C, S, and their uncertainties according to

$$S = \alpha \overline{S_{23}}/\gamma_{23} \tag{22a}$$

$$G_s = \alpha \overline{G_{total}} \quad \text{or} \quad R_s = \overline{R_{total}}/\alpha \tag{22b}$$

$$R_C \equiv R_{C1} + R_{C2} = \overline{R_{total}} - R_S \tag{22c}$$

and

$$\frac{U_S}{S} = \sqrt{\left(\frac{U_{\overline{S_{23}}}}{\overline{S_{23}}}\right)^2 + \left(\frac{U_\alpha}{\alpha}\right)^2 + \left(\frac{U_{\gamma_{23}}}{\gamma_{23}}\right)^2} \qquad (23a)$$

$$\frac{U_{G_S}}{G_S} = \sqrt{\left(\frac{U_{\overline{G_{total}}}}{\overline{G_{total}}}\right)^2 + \left(\frac{U_\alpha}{\alpha}\right)^2} \qquad (23b)$$

$$U_{R_C} = \sqrt{\left(U_{\overline{R_{total}}}\right)^2 + \left(U_{R_S}\right)^2} = \sqrt{\left(\frac{U_{\overline{G_{total}}}}{\overline{G_{total}}}R_{total}\right)^2 + \left(\frac{U_{G_S}}{G_S}R_S\right)^2} \qquad (23c)$$

A Matlab code GamaAlpha can be used to calculate U_α and $U_{\gamma_{23}}$ and the following. All the lengths and their uncertainties are shown in Fig. 6.

$$\frac{U_S}{S} = \sqrt{\left(\frac{U_{S_{23}}}{S_{23}}\right)^2 + \left(\frac{U_\alpha}{\alpha}\right)^2 + \left(\frac{U_{\gamma_{23}}}{\gamma_{23}}\right)^2} \qquad (24a)$$

$$\frac{U_{G_S}}{G_S} = \sqrt{\left(\frac{U_{G_{total}}}{G_{total}}\right)^2 + \left(\frac{U_\alpha}{\alpha}\right)^2} \qquad (24b)$$

$$U_{R_C} = \sqrt{\left(U_{R_{total}}\right)^2 + \left(U_{R_S}\right)^2} = \sqrt{\left(\frac{U_{G_{total}}}{G_{total}}R_{total}\right)^2 + \left(\frac{U_{G_S}}{G_S}R_S\right)^2} \qquad (24c)$$

The Matlab code GamaAlpha can be used to calculate the above uncertainties. All the lengths and their uncertainties are shown in Fig. 6.

References

88

[1] Coleman, H. W., Steele, W. G., 1999, *Experimentation and Uncertainty Analysis for Engineers*, John Wiley & Sons, NY.

[2] Brown, K. K., Coleman, H. W., Steele, W. Gl., 1998, "A Methodology for Determining Experimental Uncertainties in Regressions", J. Fluids Eng. **120**, pp. 445-456.

Bibliography

Boukai, A. I., Bunimovich, Y., Tahir-Kheli, J., Yu, J.-K., Goddard Iii, W. A., and Heath, J. R. 2008. "Silicon nanowires as efficient thermoelectric materials". *Nature* 451**:**168-171.

Broido, D. A., and Reinecke, T. L. 1995. "Effect of superlattice structure on the thermoelectric figure of merit". *Physical Review B* 51**:**13797.

Broido, D. A., and Reinecke, T. L. 2001. "Theory of thermoelectric power factor in quantum well and quantum wire superlattices". *Physical Review B* 64**:**045324.

Broido, D. A., and Reinecke, T. L. 1997. "Thermoelectric transport in quantum well superlattices". *Applied Physics Letters* 70**:**2834-2836.

Cahill, D. G. 2004. "Analysis of heat flow in layered structures for time-domain thermoreflectance". *Review of Scientific Instruments* 75**:**5119-5122.

Cahill, D. G. 1990. "Thermal-Conductivity Measurement from 30-K to 750-K - the 3-Omega Method". *Review of Scientific Instruments* 61**:**802-808.

Chen, G. 2005. "Nanoscale Energy Transport and Conversion: A Parallel Treatment of Elections, Molecules, Phonons, and Photons", 1st ed, vol. Oxford University Press.

Chen, G., and Shakouri, A. 2002. "Heat Transfer in Nanostructures for Solid-State Energy Conversion". *Journal of Heat Transfer-Transactions of the Asme* 124**:**242-252.

Chen, R., Hochbaum, A. I., Murphy, P., Moore, J., Yang, P., and Majumdar, A. 2008. "Thermal Conductance of Thin Silicon Nanowires". *Physical Review Letters* 101**:**105501-4.

Chiritescu, C., Cahill, D. G., Heideman, C., Lin, Q., Mortensen, C., Nguyen, N. T., Johnson, D., Rostek, R., and Bottner, H. 2008. "Low thermal conductivity in nanoscale layered materials synthesized by the method of modulated elemental reactants". *Journal of Applied Physics* 104**:**033533-5.

Chiritescu, C., Cahill, D. G., Nguyen, N., Johnson, D., Bodapati, A., Keblinski, P., and Zschack, P. 2007. "Ultralow Thermal Conductivity in Disordered, Layered WSe2 Crystals". *Science* 315**:**351-353.

Choi, T. Y., Poulikakos, D., Tharian, J., and Sennhauser, U. 2005. "Measurement of thermal conductivity of individual multiwalled carbon nanotubes by the 3-omega method". *Applied Physics Letters* 87**:**-.

Cronin, S. B., Lin, Y. M., Black, M. R., Rabin, O., and Dresselhaus, M. S. 2002. "Thermoelectric transport properties of single bismuth nanowires". *Proceedings ICT '02. 21st International Conference on Thermoelectrics.***:**243-248.

Datta, S., Pepper, M., and Ahmad, H. 1995. "Electronic Transport in Mesoscopic Systems", vol. Cambridge University Press.

Fleurial, J. P., Gailliard, L., Triboulet, R., Scherrer, H., and Scherrer, S. 1988. "Thermal properties of high quality single crystals of bismuth telluride--Part I: Experimental characterization". *Journal of Physics and Chemistry of Solids* 49**:**1237-1247.

Harman, T. C., Taylor, P. J., Walsh, M. P., and LaForge, B. E. 2002. "Quantum Dot Superlattice Thermoelectric Materials and Devices. (Cover story)". *Science* 297**:**2229.

Heideman, C., Nyugen, N., Hanni, J., Lin, Q., Duncombe, S., Johnson, D. C., and Zschack, P. 2008. "The synthesis and characterization of new [(BiSe)1.10]m[NbSe2]n, [(PbSe)1.10]m[NbSe2]n, [(CeSe)1.14]m[NbSe2]n and [(PbSe)1.12]m[TaSe2]n misfit layered compounds". *Journal of Solid State Chemistry* 181**:**1701-1706.

Heremans, J., and Thrush, C. M. 1999. "Thermoelectric power of bismuth nanowires". *Physical Review B* 59**:**12579.

Heremans, J. P., Jovovic, V., Toberer, E. S., Saramat, A., Kurosaki, K., Charoenphakdee, A., Yamanaka, S., and Snyder, G. J. 2008. "Enhancement of Thermoelectric Efficiency in PbTe by Distortion of the Electronic Density of States". *Science* 321**:**554-557.

Hicks, L. D., and Dresselhaus, M. S. 1993. "Effect of quantum-well structures on the thermoelectric figure of merit". *Physical Review B* 47**:**12727.

Hicks, L. D., and Dresselhaus, M. S. 1993. "Thermoelectric figure of merit of a one-dimensional conductor". *Physical Review B* 47**:**16631.

Hochbaum, A. I., Chen, R., Delgado, R. D., Liang, W., Garnett, E. C., Najarian, M., Majumdar, A., and Yang, P. 2008. "Enhanced thermoelectric performance of rough silicon nanowires". *Nature* 451**:**163-167.

Hsu, K. F., Loo, S., Guo, F., Chen, W., Dyck, J. S., Uher, C., Hogan, T., Polychroniadis, E. K., and Kanatzidis, M. G. 2004. "Cubic AgPbmSbTe2+m: Bulk Thermoelectric Materials with High Figure of Merit". 303**:**818-821.

Incropera, F. P. 2007. "Introduction to heat transfer", 5th ed, vol. Wiley, Hoboken, N.J.

Jin, C. G., Xiang, X. Q., Jia, C., Liu, W. F., Cai, W. L., Yao, L. Z., and Li, X. G. 2004. "Electrochemical fabrication of large-area, ordered Bi2Te3 nanowire arrays". *Journal of Physical Chemistry B* 108**:**1844-1847.

Ju, Y. S., and Goodson, K. E. 1999. "Phonon scattering in silicon films with thickness of order 100 nm". *Applied Physics Letters* 74**:**3005-3007.

Ju, Y. S., Kurabayashi, K., and Goodson, K. E. 1999. "Thermal characterization of anisotropic thin dielectric films using harmonic Joule heating". *Thin Solid Films* 339**:**160-164.

Kim, P., Shi, L., Majumdar, A., and McEuen, P. L. 2001. "Thermal transport measurements of individual multiwalled nanotubes". *Physical Review Letters* 8721**:**4.

Kim, W., Zide, J., Gossard, A., Klenov, D., Stemmer, S., Shakouri, A., and Majumdar, A. 2006. "Thermal Conductivity Reduction and Thermoelectric Figure of Merit Increase by Embedding Nanoparticles in Crystalline Semiconductors". *Physical Review Letters* 96**:**045901-4.

Li, D. Y., Wu, Y., Fan, R., Yang, P. D., and Majumdar, A. 2003. "Thermal conductivity of Si/SiGe superlattice nanowires". *Applied Physics Letters* 83**:**3186-3188.

Li, D. Y., Wu, Y. Y., Kim, P., Shi, L., Yang, P. D., and Majumdar, A. 2003. "Thermal conductivity of individual silicon nanowires". *Applied Physics Letters* 83**:**2934-2936.

Lijadi, M., David, C., and Pelouard, J.-L. 2005. "Controlled Etching of InGaAlAs and GaAsSb Using Citric Acid/Hydrogen Peroxide Mixtures". *Electrochemical and Solid-State Letters* 8**:**C189-C192.

Lin-Chung, P. J., and Reinecke, T. L. 1995. "Thermoelectric figure of merit of composite superlattice systems". *Physical Review B* 51**:**13244.

Lin, Q., Heideman, C. L., Nquyen, N., Zschack, P., Chiritescu, C., Cahill, D. G., and Johnson, D. C. 2008. "Designed Synthesis of Families of Misfit-Layered Compounds". *European Journal of Inorganic Chemistry* 2008**:**2382-2385.

Lin, Y.-M., Sun, X., and Dresselhaus, M. S. 2000. "Theoretical investigation of thermoelectric transport properties of cylindrical Bi nanowires". *Physical Review B* 62**:**4610.

Lin, Y. M., Rabin, O., Cronin, S. B., Ying, J. Y., and Dresselhaus, M. S. 2002. "Semimetal-semiconductor transition in Bi1-xSbx alloy nanowires and their thermoelectric properties". *Applied Physics Letters* 81**:**2403-2405.

Lippmann, G., Kästner, P., and Wanninger, W. 1971. "Elastic constants of PbSe". *Physica Status Solidi A* 6**:**K159-K161.

Liu, W., and Asheghi, M. 2006. "Thermal Conductivity Measurements of Ultra-Thin Single Crystal Silicon Layers". *Journal of Heat Transfer* 128**:**75-83.

Lu, L., Yi, W., and Zhang, D. L. 2001. "3 omega method for specific heat and thermal conductivity measurements". *Review of Scientific Instruments* 72**:**2996-3003.

Mavrokefalos, A., Ngoc, T. N., Michael, T. P., David, C. J., and Li, S. 2007. "In-plane thermal conductivity of disordered layered WSe_2 and $(W)_x(WSe_2)_y$ superlattice films". *Applied Physics Letters* 91**:**171912.

Mavrokefalos, A., Pettes, M. T., Zhou, F., and Shi, L. 2007. "Four-probe measurements of the in-plane thermoelectric properties of nanofilms". *Review of Scientific Instruments* 78**:**034901-6.

Mingo, N. 2004. "Thermoelectric figure of merit and maximum power factor in III--V semiconductor nanowires". *Applied Physics Letters* 84**:**2652-2654.

Moore, A. L., Saha, S. K., Prasher, R. S., and Shi, L. 2008. "Phonon backscattering and thermal conductivity suppression in sawtooth nanowires". *Applied Physics Letters* 93**:**083112-3.

Noh, M., Johnson, C. D., Hornbostel, M. D., Thiel, J., and Johnson, D. C. 1996. Control of Reaction Pathway and the Nanostructure of Final Products through the Design of Modulated Elemental Reactants, p. 1625-1635. vol. 8.

Rowe, D. M. 1995. "CRC handbook of thermoelectrics", vol.

Seol, J. H., Moore, A. L., Saha, S. K., Zhou, F., Shi, L., Ye, Q. L., Scheffler, R., Mingo, N., and Yamada, T. 2007. "Measurement and analysis of thermopower and electrical conductivity of an indium antimonide nanowire from a vapor-liquid-solid method". *Journal of Applied Physics* 101**:**023706-6.

Shi, L., Li, D. Y., Yu, C. H., Jang, W. Y., Kim, D., Yao, Z., Kim, P., and Majumdar, A. 2003. "Measuring thermal and thermoelectric properties of one-dimensional nanostructures using a microfabricated device". *Journal of Heat Transfer-Transactions of the Asme* 125**:**881-888.

Shi, L., Yu, C. H., and Zhou, J. H. 2005. "Thermal characterization and sensor applications of one-dimensional nanostructures employing microelectromechanical systems". *Journal of Physical Chemistry B* 109**:**22102-22111.

Small, J. P., Perez, K. M., and Kim, P. 2003. "Modulation of thermoelectric power of individual carbon nanotubes". *Physical Review Letters* 91**:**-.

Venkatasubramanian, R., Siivola, E., Colpitts, T., and O'Quinn, B. 2001. "Thin-film thermoelectric devices with high room-temperature figures of merit". *Nature* 413**:**597-602.

Yi, W., Lu, L., Zhang, D. L., Pan, Z. W., and Xie, S. S. 1999. "Linear specific heat of carbon nanotubes". *Physical Review B* 59**:**R9015-R9018.

Yoo, B. Y., Huang, C. K., Lim, J. R., Herman, J., Ryan, M. A., Fleurial, J. P., and Myung, N. V. 2005. "Electrochemically deposited thermoelectric n-type Bi2Te3 thin films". *Electrochimica Acta* 50**:**4371-4377.

Yu, C. H., Saha, S., Zhou, J. H., Shi, L., Cassell, A. M., Cruden, B. A., Ngo, Q., and Li, J. 2006. "Thermal contact resistance and thermal conductivity of a carbon nanofiber". *Journal of Heat Transfer-Transactions of the Asme* 128**:**234-239.

Yu, C. H., Shi, L., Yao, Z., Li, D. Y., and Majumdar, A. 2005. "Thermal conductance and thermopower of an individual single-wall carbon nanotube". *Nano Letters* 5**:**1842-1846.

Zeng, G., Bahk, J.-H., Bowers, J. E., Zide, J. M. O., Gossard, A. C., Bian, Z., Singh, R., Shakouri, A., Kim, W., Singer, S. L., and Majumdar, A. 2007. "ErAs:(InGaAs)$_{1-x}$(InAlAs)$_x$ alloy power generator modules". *Applied Physics Letters* 91**:**263510-3.

Zhou, F., Szczech, J., Pettes, M. T., Moore, A. L., Jin, S., and Shi, L. 2007. "Determination of Transport Properties in Chromium Disilicide Nanowires via Combined Thermoelectric and Structural Characterizations". *Nano Letters* 7**:**1649-1654.

Zhou, J., Jin, C., Seol, J. H., Li, X., and Shi, L. 2005. "Thermoelectric properties of individual electrodeposited bismuth telluride nanowires". *Applied Physics Letters* 87**:**133109.

Zide, J. M., Klenov, D. O., Stemmer, S., Gossard, A. C., Zeng, G., Bowers, J. E., Vashaee, D., and Shakouri, A. 2005. "Thermoelectric power factor in semiconductors with buried epitaxial semimetallic nanoparticles". *Applied Physics Letters* 87**:**112102-3.

Ziman, J. M. 1960. "Electrons and Phonons: The Theory of Transport Phenomena in Solids", vol. Oxford University Press.

Zink, B. L., Revaz, B., Cherry, J. J., and Hellman, F. 2005. "Measurement of thermal conductivity of thin films with a Si-N membrane-based microcalorimeter". *Review of Scientific Instruments* 76**:**024901-5.

VITA

Anastassios Andres Mavrokefalos was born in Nicosia, Cyprus on April 10, 1977, the son of Andreas Mavrokefalos and Ioulia Mavrokefalou. After completing work at the Pancyprium Gymnasium in 1995, he entered the Higher Technical Institute in Nicosia Cyprus. After receiving his Technical Degree in 1998 he was drafted in the Technical Corps of the Cyprus National Guard where he was dismissed as a Second Lieutenant in 2000. Following that he entered the University of Texas at Austin where he received his degree in Bachelors of Science in Mechanical Engineering in May 2002. During the following year he was employed as a Mechanical Engineering at Thermofast Ltd in Nicosia Cyprus. In August 2003 he entered the Graduate School of The University of Texas at Austin and received the degree of Masters of Science from the University of Texas at Austin in December 2005. In January 2006 he entered the doctoral program in Mechanical Engineering Department at the University of Texas at Austin.

Permanent address: 1, Grigoriou Ksenopoulou Str., Egkomi, Nicosia 2402, Cyprus

This Dissertation was typed by the author